Air Force Institute of Technology

AFIT Scholar

3-14-2008

Demonstration of a Strategy to Perform Two-Dimensional Diode Laser Tomography

Ryan N. Givens

Follow this and additional works at: https://scholar.afit.edu/etd

⊙ Part of the Plasma and Beam Physics Commons, and the Thermodynamics Commons

**DEMONSTRATION OF A STRATEGY TO PERFORM TWO-DIMENSIONAL
DIODE LASER TOMOGRAPHY**

THESIS

Ryan N. Givens, Captain, USAF

AFIT/GAP/ENP/08-M04

DEPARTMENT OF THE AIR FORCE
AIR UNIVERSITY

AIR FORCE INSTITUTE OF TECHNOLOGY

Wright-Patterson Air Force Base, Ohio

APPROVED FOR PUBLIC RELEASE, DISTRIBUTION UNLIMITED

The views expressed in this thesis are those of the author and do not reflect the official policy or position of the United States Air Force, Department of Defense, or the United States Government.

AFIT/GAP/ENP/08-M04

DEMONSTRATION OF A STRATEGY TO PERFORM TWO-DIMENSIONAL
DIODE LASER TOMOGRAPHY

THESIS

Presented to the Faculty

Department of Engineering Physics

Graduate School of Engineering and Management

Air Force Institute of Technology

Air University

Air Education and Training Command

In Partial Fulfillment of the Requirements for the

Degree of Master of Science

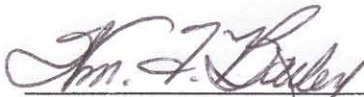Ryan N. Givens, BS, MSBA

Captain, USAF

March 2008

APPROVED FOR PUBLIC RELEASE; DISTRIBUTION UNLIMITED

AFIT/GAP/ENP/08-M04

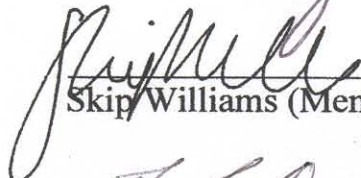# DEMONSTRATION OF A STRATEGY TO PERFORM TWO-DIMENSIONAL DIODE LASER TOMOGRAPHY

Ryan N. Givens, BS, MSBA
Captain, USAF

Approved:

_____
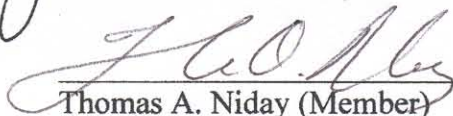William F. Bailey (Chairman)

14 Mar '08
Date

_____
Skip Williams (Member)

26 Feb 2008
Date

_____
Thomas A. Niday (Member)

14 Mar 08
Date

Abstract

Demonstration of a strategy to perform two-dimensional diode laser tomography using *a priori* knowledge from symmetry arguments and computational fluid dynamic (CFD) calculations is presented for a flat flame burner. The strategy uses an optimization technique to determine flame diameter and location using a vector quantization approach. Next, the variance in a training set, produced from CFD calculations, is captured using principal components analysis. The information in the training set allows interpolation between beam paths resulting in temperature and density maps. Finally, the TDLAS temperature and density maps are shown to agree with traditional thermocouple measurements of the flat flame burner to within five percent. Preliminary tomography results using the same strategy are then presented for a super-sonic flow through an isolator, a length of wind tunnel necessary to keep the shock wave produced by the combustor from reaching the inlet.

To my wife

Acknowledgements

Many people contributed to the success of this project. First I would like to extend my sincere thanks to Dr. Skip Williams. His insight, advice, and ability to keep me on the right track were invaluable not only to the completion of this thesis, but also to my comprehension of the scientific process. I lost count of the times I needed redirection and he was there to help me out. Special thanks are also due to Dr. William Bailey for his overall guidance of this thesis and specifically for his insistence that I have a sound understanding of the theory behind the experiment. I always came away from our meetings determined to understand more, and hopefully that shows in this final product. I would also like to thank Dr. Chad Lindstrom for his patience with my daily questioning and his amazing ability to somehow instantly find the errors in my thought processes that would have kept me stuck for days. In addition, I am very grateful to Major Thomas Niday for agreeing to be on my committee.

I would like to offer my genuine gratitude to Bill Terry for all of his work setting up the burner experiments as well as Doug Davis and Chung-Jen Tam for providing CFD simulations. To the RC 18 crew, thank you for allowing me to join in on the data collections. I learned a great deal about what it takes to run experiments of that magnitude.

Finally, I would like to thank my wife. Thank you for pushing me. Thank you for sympathizing with me. Thank you for loving me. Nothing ever seemed too bad as long as I remembered I had you to come home to.

<div align="right">Ryan N. Givens</div>

Table of Contents

List of Figures

List of Tables

List of Symbols

The following notation will be used throughout this thesis:

NOTATION	DEFINITION	PAGE
h	Planck's constant	12
c	Speed of light in a vacuum	12
f, g, h	Inter-atomic distances in the water molecule	12
$I_x, I_{,y}, I_z, I_A, I_B, I_C$	Moment of inertia where the subscript denotes the axis about which the moment of inertia is respect to	12
m_O, m_H	Masses of oxygen and hydrogen respectively	12
u	Atomic mass unit	12
Å	Angstrom	12
J_0, J_1	The the total angular momentum of the water molecule for the initial and final states	15
S'	HITRAN line intensity	13, 17-18, 21, 46-47
q(T)	Partition function of the water molecule	13, 17, 20-21
ν, ν_{10}	Transition frequency	13, ...
k	Boltzmann constant	13, ...
ε_0	Permittivity of free space	13, ...
T, T_{REF}	Temperature and reference temperature used to determine HITRAN line intensities	13, 17-18, 21, ...
M_0, M_1	Projection of J onto the lab reference frame	15
E_0	Ground state, or term energy	13, 17, ...
λ	Transition wavelength	14
N_0, N_1, N_T	Population of the ground state, excited state, and total species concentration respectively	13, 17-18, 21, 46, ...
ρ	Incoming radiation density	14-16
$B_{1\rightarrow0}, B_{1\leftarrow0}$	Einstein coefficients form stimulated emission and absorption, respectively	14-16
g_0, g_1	Degeneracies of the ground and excited states	13, ...
S_{10}	Line strength of a transition	13, ...
$g(\nu-\nu_{10}), g(\nu)$	Lineshape function of a transition	15-17, ...
σ	Transition cross section	15-17
F	Incident flux	15-17
μ	Dipole moment operator	15
R_{10}	Weighted square of the transition moment	17
I, I_0	Intensity after passing through a gas and original intensity	16, 48
ℓ	Length	13, ...
$\Delta\nu_{1/2}$	Full width at half maximum of Lorentzian contribution to the Voigt lineshape	21
b	Pressure broadening coefficient	21

Notation	Definition	Page
$p(s,\theta)_i$, $\vec{p}$	The ith path integral from the ith line of sight and the matrix of line of sight measurements	26-27
α, $\hat{\alpha}$	Absorption coefficient of a transition and the approximated absorption coefficient obtained using tomography	26-27
δ	Dirac delta function	26-27
$\Re_i$, $\Re$	Radon transform of the ith projection which forms the projection matrix $\Re$	26-27
w_{ij}	Amount of area of a pixel of the absorption coefficient map traversed by the ith line of sight	26-27
q_j, $\vec{q}$	The jth basis image and the array of basis images used to reconstruct the line of sight data	26-27
q_{rad}, q_{conv}	Radiative heat transfer due to radiation and convection	32-33
ε	Emissivity of a bead at the tip of a thermocouple	32-33
A	Surface area of a bead at the tip of a thermocouple	32-33
σ_{SB}	The Stefan-Boltzmann constant	32-33
h_{conv}	The convective heat transfer coefficient between a gas flow and a bead	32-33
T_b, T_g, T_∞	The temperatures of a bead, gas, and room respectively	32-33
$d(m)$	The diameter of a bead	32-33
N	The Nusselt number for a gas a bead	32-33
k_{tc}	The gas thermal conductivity	32-33
P	Prandtl number	32-33
R	Reynolds number	32-33
ρ_g	gas density	32-33
U	gas velocity	32-33
μ_v	gas viscosity	32-33
A_T, A_H, A_C	Spectrum from total line of sight, hot contribution, and cold contribution respectively	48
L, L_C, d	Total path length, cold path length, and hot path length respectively	48
D	Diameter of the flat flame burner	48

DEMONSTRATION OF A STRATEGY TO PERFORM TWO-DIMENSIONAL DIODE LASER TOMOGRAPHY

I   Introduction

Background

Since the mid 1990s, groups have used tunable diode laser absorption spectroscopy (TDLAS) to determine density, pressure, temperature, and velocity of gases.[1] TDLAS uses a spectrally narrow, tunable laser source to scan an absorption feature of a particular gas. The ability to measure gas density, pressure, temperature, and velocity in the flow of a supersonic combustion ramjet (scramjet) engine would allow engine performance to be monitored. Optimizing engine performance in a scramjet presents many technical challenges including determination of mass capture as a function of vehicle attitude and condition in the inlet of the engine; ignition, flame holding, and fuel injection in the combustor; and maximizing combustion efficiency and thrust generation in the exhaust plane.[2] Although other techniques exist for obtaining information about the flow, TDLAS can be used to monitor all of these variables in ground tests and also has the potential to be miniaturized for flight vehicles.

Alternative techniques involving probe and wall measurements, while proven, do not necessarily provide a complete picture of the flow.[3] Wall measurements are limited to pressure and temperature readings at the boundary of the flow. Computational fluid dynamic (CFD) calculations and probe measurements show that flow conditions vary

1

greatly from the core of the flow to the extremities. TDLAS improves upon wall measurements by providing an average measurement across the entire line of sight thus providing information in the core of the flow. Probe measurements are beneficial in that they can be moved or built in an array to investigate conditions throughout the flow. However, their presence perturbs the flow necessitating a correction to the measurement. TLDAS does not have this drawback because passing a laser through the flow does not disrupt the flow.

TDLAS, therefore, provides another avenue for collecting information about the flow. By passing a beam through the flow, a line of sight absorption measurement is possible. By carefully choosing the laser wavelengths to correspond to species-specific absorption features, of water in the case of this study, a variety of flow properties can be determined. Three lasers with nominal center wavelengths of 1391, 1392, and 1397 nm were used along each line of sight in this experiment. The shape and intensity of the absorption features in each of the three spectra yielded information regarding temperature and pressure as well as the density and velocity of the species in the probed area of the flow.[3]

Line of sight measurements are limited, however, in that the information gained is averaged along the path of the beam. With a single beam path, therefore, no spatial information about the flow can be obtained. One solution to gathering spatially resolved information of the flow from the line of sight measurements is to add more beam paths. Tomography, similar to that used in an MRI or CAT scan, is then performed by combining the information of multiple beam paths. Unfortunately, methods like these generally require hundreds of beam paths to gain the resolution necessary to extract

2

contour information – a solution which is not feasible in flight environments or even most ground tests. To overcome this problem, reduction in the number of beam paths necessary to perform tomography can be accomplished through the use of contour information gained from CFD computations or planar laser-induced fluorescence (PLIF) experiments. By assuming the model gained from CFD or PLIF provides a good approximation of the relative variation in the flow properties, the model can be fit to the TDLAS line of sight information through a least squares fitting method, allowing intelligent interpolation between the beam paths. Through this process of two-dimensional tomography, spatially and temporally resolved, quantitative information about the flow can be obtained.[3, 4]

Problem Statement

The overall purpose of this project was to investigate the possibility of reducing the number of lines of sight required to perform tomography using *a priori* knowledge gained from symmetry arguments or CFD calculations. To fulfill this purpose, the temperature and water concentration of a flame provided by a flat flame, McKenna type burner were measured six millimeters above the surface of the burner through the traditional method of thermocouples as well as a pressure and relative humidity probe. The flat flame burner consists of a circular, porous copper region, six centimeters in diameter. The gas mixture, methane and air, is distributed evenly over this region and, when lit, provides a uniform, or flat, temperature profile across the area of the porous region. The results from the thermocouple measurements were compared to the tunable diode laser absorption tomography results performed using an analytic two-zone model, an optimized computational two-zone model, and finally an optimized computational

CFD model of the flat flame burner. The two-zone model, discussed in detail in Chapter IV, assumes two temperature regions for the flat flame burner experiment: an elevated temperature within the flame of the burner surrounded by room temperature air. The agreement on temperature and species concentration of the two methods, tunable diode laser absorption tomography and thermocouple measurements, provides a proof of concept for the tomography strategy which was employed. This same strategy was then applied to an experiment to perform tunable diode laser absorption tomography (TDLAT) on a vitiated supersonic flow through an isolator. Preliminary results are discussed in Chapter V.

The two-zone model was used in the implementation of two methods to determine temperature and species concentration. The first method, called the two-zone analytic method, uses TDLAS data from seven beam paths, the positions of the lines of sight relative to the burner, and two assumptions about the burner: the flat flame burner provides a flat temperature profile, and the flame is circular. Employing some algebra and geometry, detailed in Chapter IV, the temperature in the center of the flame was found to be within 10 K of the thermocouple measurements. The second method, called the two-zone computational method, used the same data, beam path measurements, and assumptions about the burner to obtain the same temperature and water concentration results computationally. In the computational method, the two-zone model provided a basis image which was scaled to fit the TDLAS data using a least squares method also detailed in Chapter IV. These two methods are intended to step the reader through a basic application of tomography using a basis derived from *a priori* knowledge. Both of these methods agreed with the thermocouple temperature measurements and species

4

concentration calculations to within five percent for the interior of the flame and the surrounding room air, but because they use the two-zone model, they do not provide any information at the boundary layer of the flame. The two-zone model assumes an instantaneous temperature change at the boundary between the surrounding room temperature gas and the hot circular flame. To obtain better agreement with the thermocouple measurements in this region, either more beam paths along with a model with more temperature zones or a better understanding of how to interpolate between the beam paths was necessary. CFD calculations were used to provide this information.

The CFD model provided the information to allow interpolation between lines of sight, thus obtaining spatially resolved temperature and species concentration maps of the flat flame burner. Although the temperature and diameter of the CFD calculations did not agree with thermocouple measurements, the shape of the temperature profile in the boundary region showed good agreement with the thermocouple data. By scaling the CFD model to represent a range of peak temperatures and peak species concentrations of the burner, a training set was developed for each of the water absorption features used for temperature and species concentration determination. The training sets for each of the absorption features consisted of a series of maps of the frequency integrated absorption coefficients for a range of scaled temperatures and species concentration.

Two algorithms were proposed to find the optimum basis set from the training set: vector quantization (VQ) and principal components analysis (PCA).[5, 6] Both of these algorithms can be found in Appendix C in the programs Create_VQbasis and Create_basisv2, respectively. While PCA performed well in the creation of basis sets, VQ showed limited utility for the flat flame burner. Instead, VQ was used to optimize

the fits to the two models, to aid in providing averages in time-resolved oscillations in the isolator experiment, and to create a basis for the near real-time tomography performed during data collection for the isolator experiment. PCA was used to create the basis sets, capturing variance in each training set and resulting in a basis set which could be reduced in size.[5] A least squares approach was used to fit the CFD basis sets to the TDLAS measurements. The basis sets were then added in linear combination resulting in a tomographic map which agreed with the TDLAS data from the multiple lines of sight.

The PCA was performed because the CFD models covering all of the possible states could be very large, thus requiring many lines of sight to make the fit well defined. To reduce the number of lines of sight necessary, PCA was used on the training sets to create much smaller basis sets which still represented the majority of possible conditions of the flow yet maintained a well posed mathematical problem with fewer lines of sight. The compression of the training sets was possible due to the high degree of redundancy in the varied conditions of the CFD models. The research questions under investigation for this thesis were how to create the best possible basis set from the CFD models and how to obtain the best possible fit of the measured TDLAS data to the basis set while still maintaining a well conditioned problem.

Scope

This thesis investigated a strategy to perform tomography of a flat flame burner and vitiated super-sonic flow using TDLAS measurements from multiple lines of sight resulting in quantitative temperature, density, and pressure maps. Temperature and species concentration maps of the flat flame burner, obtained using tomography were compared to a thermocouple temperature profile and calculated species concentrations of

6

the flame. This comparison provided verification for the fit of the TDLAS measurements to the two-zone and CFD models. The favorable comparisons of both the temperature and species concentration obtained using tomography to those obtained using thermocouples lend added credibility to the optimized fitting routine applied to the super-sonic flow data by Lindstrom.[3] Preliminary results for the super-sonic flow are presented in chapter 6.

Objectives

In this thesis, the following objectives were accomplished:

i.   Verify the utility of TDLAS for the flat flame burner by comparing with thermocouple measurements.

ii.   Investigate the number of beam paths required to achieve accurate tomographic temperature and density maps for the flat flame burner.

iii. Evaluate the performance of PCA in reducing the dimensionality of training sets and enabling tomography with a limited number of beam paths.

iv.   Provide a proof of concept for the application of TDLAT performed with limited optical access in more complicated flows.

Approach/Methodology

A temperature profile of a flat flame burner measured with thermocouples was used as a comparison for the TDLAT. Tomography was performed using both the two-zone model as well as the CFD model using the data from 7, 63, and 119 lines of sight for each model. This provided a proof of concept for the strategy developed to perform two-

7

dimensional tomography of the flat flame burner. The proof of concept was used to provide confidence in the tomography results performed on the isolator data.

Equipment and Materials

The flat flame burner experiments were performed in the Propulsion Directorate of the Air Force Research Laboratory at Wright-Patterson Air Force Base. The first experiment measured the temperature profile of a flat flame, McKenna type burner using an array of three type B thermocouples of varying bead and wire diameters and two type K thermocouples. The second burner experiment was performed with an array of tunable diode lasers and the required data acquisition system to measure water absorption features which were used to obtain a similar temperature profile.

The isolator experiments were performed in Research Cell 18 at Wright-Patterson Air Force Base. These experiments used the same tunable diode lasers and data acquisition system as the TDLAS burner experiment to measure water absorption in the flow through the isolator portion of a supersonic wind tunnel.

Data processing and tomography were performed on a standard desktop computer with a 2.39 GHz processor and 2.0 GB of RAM. Algorithm development was accomplished primarily in Matlab, though the Igor curve fitting suite was used to process the raw data from the tunable diode lasers.[7]

Preview

The remainder of this thesis is organized into five chapters. Chapter 2 provides the necessary spectroscopic background and theory to obtain a tomographic temperature map from raw TDLAS measurements. Chapters 3, 4, and 5 provide the background,

experimental setup, and results for each of the three experiments: the flat flame thermocouple experiment, the flat flame TDLAT experiment, and the isolator TDLAT experiment. Chapter 3 explains the traditional thermocouple methods used to obtain a temperature profile for the flat flame burner. The results of the thermocouple measurements provide a point of comparison for the remaining TDLAS measurements and tomography. Chapter 4 includes the results for both the thermocouple and TDLAS experiments on the flat flame burner along with the comparison of the two. This comparison validates the strategy implemented to perform two-dimensional tomography on a flow. Chapter 5 provides the preliminary results of the isolator experiment which employed the same strategy to perform two-dimensional tomography as the flat flame burner. Using only line of sight TDLAS measurements, the CFD was shown to be missing the first reflection in the shock train. Due to this inaccuracy in the CFD calculations for the isolator, optimization techniques used in the flat flame experiment to determine diameter and center location were modified to adjust the shock shape, location, and wall thickness in the isolator CFD model. The resulting fits to the isolator TDLAS data are presented. The thesis concludes with Chapter 6 where a summary, overview of future studies, and recommendations for future research are discussed.

II Theory

Introduction

This chapter develops the theory behind TDLAS and the tomography performed using TDLAS measurements. It begins with a description of the water molecule vibrational and rotational energy levels that provide the transitions which were used for TDLAS. Next, Beer's law is presented. It governs the absorption of light by the water transitions. The chapter then provides an overview of the spectroscopic background material necessary to understand TDLAS. Finally, a discussion of tomography as it is applied to this thesis is presented.

The Water Molecule

The burner and isolator experiments rely on absorption spectra which are the result of the absorption of laser light by water molecules in a flow. As the laser is tuned through a frequency range, transitions in the water molecule attenuate the light according to the temperature and concentration of the water molecules. Water was selected as the species of measurement due to its abundance of transitions in the range of wavelengths where commercial telecommunications lasers have been developed. From thermodynamics, molecules have 3N degrees of freedom where N is the number of atoms in the molecule. For the water molecule, three of its nine degrees of freedom are translational and three are rotational, leaving three vibrational modes. Each vibrational state is composed of many rotational states. The figure below, adapted from Bernath, shows the vibrational modes of the water molecule.[8]

10

v_1 3651 cm^{-1}
symmetric stretch

v_2 1595 cm^{-1} bend

v_3 3756 cm^{-1}
antisymmetric stretch
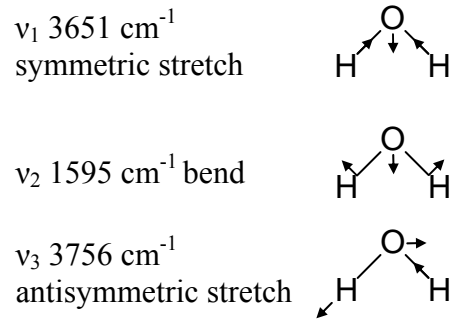
Figure 1. The normal modes of vibration of H_2O

While many water vibrational transitions exist within the wavelength range of the lasers used, the transitions used in this research occurred between rotational levels in the 000 and 101 vibrational transition. The three numbers in the vibrational level labeling scheme refer to the quanta of energy in each of the vibrational modes, symmetric stretch, bend, and antisymmetric stretch respectively.[8] The transition from 000 to 101, therefore, indicates that the absorption features used were the result of incident light exciting water molecules from their vibrational ground state to an excited state with one quanta of symmetric stretch and one quanta of antisymmetric stretch.

Specific rotational transitions of the 000 to 101 vibrational transition were selected based on the population density, obtained using Boltzmann statistics, of the ground vibrational state. For the molecule to absorb light at a transition, it must have a population in the initial state. Thus, transitions were selected based on the population of the initial state over the expected temperature range of the experiment.

In rotational spectroscopy, energy levels are referred to by their total angular momentum, J, and the projection of the total angular momentum on the molecular axis of highest symmetry, z. As shown below in the figure adapted from Bernath, water is a planar molecule where the highest degree of rotational symmetry is about the 180°

11

rotationally symmetric axis through the oxygen atom in the plane of the molecule.[8]
For a planar molecule, the x-axis is chosen to be out of the plane.
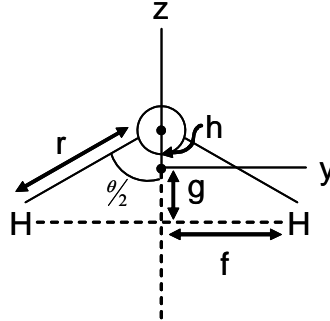
Figure 2. The water molecule

The origin, which defines the distances f, g, and h, is chosen to be the center of mass of
the molecule. The moments of inertia for the rigid rotor model of the water molecule are
therefore:

$$
\begin{aligned}
I_z &= 2m_H f^2 \\
I_y &= m_O h^2 + 2m_H g^2 \\
I_x &= I_z + I_y = m_O h^2 + 2m_H (g^2 + f^2)
\end{aligned}
\tag{1}
$$

Axes are also labeled according to the magnitude of their respective moments of inertia
such that

$$
I_A \le I_B \le I_C . \tag{2}
$$

In the case of H_2O where r = .0958 Å, θ = 104.5°, m_H = 1.00 atomic mass unit (u), m_O =
16.00 u, f = 0.0757 Å, g = 0.5213 Å, and h = 0.0652 Å, the moments of inertia are

$$
\begin{aligned}
I_z &= 1.148 \ u\text{Å}^2 (\equiv I_B) \\
I_y &= 0.6115 \ u\text{Å}^2 (\equiv I_A) . \\
I_x &= 1.760 \ u\text{Å}^2 (\equiv I_C)
\end{aligned}
\tag{3}
$$

12

The water molecule is thus an asymmetric top because none of the moments of inertia are equal. Asymmetric tops provide a large number of transitions because the dipole moments along each of the axes, a, b, and c, are non-vanishing.[8]

Once the axes are defined, the rotational energy levels and selection rules for linear and symmetric top molecules can be developed using the Hamiltonian operator for the rigid rotor in the Schrödinger equation. In the case of asymmetric tops, however, there is no general analytical solution to the Schrödinger equation. Instead, solutions are usually found numerically.

For this research, HITRAN was used to provide the transition parameters including initial state energy, transition energy, and line intensity. HITRAN is a collection of spectroscopic parameters created by the Air Force Cambridge Research Laboratories.[9] The line intensity of a transition, S', is shown below in SI units of $m^{2-}s^{-1}$. It is proportional to the evaluation of the dipole moment operator, S_{10}, in the Schrödinger equation. It combines the probability of a transition with thermodynamic equilibrium Boltzmann statistics given by:[8]

$$S' = \frac{2\pi^2 v_{10}}{3\varepsilon_0 hcq(T)} e^{-E_0/kT} (1 - e^{-hv_{10}/kT}) S_{10} .$$
(4)

Here, v_{10} is the transition frequency between rotational levels of the ground vibrational state, 0, and the upper vibrational state, 1, h is Planck's constant, c is the speed of light, $q(T)$ is the partition function, E_0 is the energy of the initial state, or term energy, k is Boltzmann's constant, T is the temperature, and S_{10} is the line strength given by the dipole moment operator. The line intensity, S', can be related to the cross section of the transition as well as the absorption coefficient and the Einstein coefficients as shown in the next section.[8]

13

Beer's Law

When light passes through a gas, absorption or stimulated emission may occur when the energy of the incoming photons matches the energy gap between two levels. A transition from a rotational state, of the initial vibrational state to a rotational state of the excited vibrational state is shown in the figure below, adapted from Bernath.[8] The energy of the incoming photon, E, is equal to hc divided by the wavelength, λ, as shown in Figure 3.

$$E = \frac{hc}{\lambda}$$
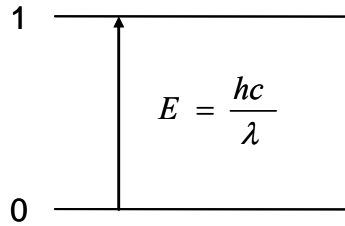
Figure 3. A transition of the water molecule from the initial state, 0 to the upper state, 1

Beer's law describes the intensity, I, of light after it passes through a distance, l, of gas. Given an incoming radiation density, ρ, and the Einstein coefficients for stimulated emission and absorption, $B_{1 \to 0}$ and $B_{1 \leftarrow 0}$, the rate equation for the upper state is:

$$\frac{dN_1}{dt} = -B_{1 \to 0}\rho N_1 + B_{1 \leftarrow 0}\rho N_0 , \qquad (5)$$

where N_1 and N_0 are the populations, given in molecules-cm^{-3}, of the excited and initial state respectively. The incoming radiation density, $\rho = h v_{10} F/c$, has units of kg-s^{-2}-m^{-1}, where h is Planck's constant in J-s, v_{10} is the transition frequency in Hz, F is the incoming flux in photons m^{-2}-s^{-1}, and c is the speed of light in m-s^{-1}. Note that the

Einstein coefficients for absorption and stimulated emission, $B_{1\to0}$ and $B_{1\leftarrow0}$, both having units of m-s-kg^{-1} from the following equation:

$$B_{1\to0} = \frac{g_0}{g_1} B_{1\leftarrow0} = \frac{2\pi^2}{3\varepsilon_0 h^2 g_1} S_{10} g(\nu - \nu_{10}),$$ (6)

where $g_0 = 2J_0 + 1$ and $g_1 = 2J_1 + 1$ are the degeneracies of state 0 and 1 with total angular momentum J_0 and J_1, ε_0 is the permittivity of free space in C^2-N^{-1}-m^{-2}, h is Planck's constant in J-s, $g(\nu-\nu_{10})$ is the lineshape function with units of seconds, and S_{10} is the line strength in C^2-m^2:

$$S_{10} = \sum_{M_1} \sum_{M_0} \left| \langle J_1 M_1 | \mu | J_0 M_0 \rangle \right|^2.$$ (7)

In Equation (7), J_0 and J_1 are the total angular momentum of a molecule in state 0 or 1 and M_0 and M_1 are the projection of J_0 and J_1 onto the lab reference frame for those states. Rearranging Equation (5) and using Equation (6) yields:

$$\frac{dN_1}{dt} = \rho B_{1\leftarrow0} (N_0 - \frac{g_0}{g_1} N_1).$$ (8)

Replacing the Einstein absorption coefficient with its definition from Equation (6) produces:

$$\frac{dN_1}{dt} = \rho \frac{2\pi^2}{3\varepsilon_0 h^2 g_0} S_{10} g(\nu - \nu_{10})(N_0 - \frac{g_0}{g_1} N_1).$$ (9)

Adding the definition of $\rho = h\nu_{10}F/c$ generates:

$$\frac{dN_1}{dt} = F \frac{2\pi^2 \nu_{10}}{3\varepsilon_0 hcg_0} S_{10} g(\nu - \nu_{10})(N_0 - \frac{g_0}{g_1} N_1).$$ (10)

Then, the cross section, σ, with units of m^2 is defined as follows:

$$\sigma = \frac{2\pi^2 S_{10}}{3\varepsilon_0 hc} \frac{\nu_{10}}{g_0} g(\nu - \nu_{10}),$$ (11)

15

with S_{10} in C^2-m^2, v_{10} in Hz, $g(v-v_{10})$ in seconds, ε_0 in C^2-N^{-1}-m^{-2}, h in J s, and c in m-s^{-1}. Substituting the cross section from Equation (11) into Equation (10) results in the form below: [8, 10]

$$\frac{dN_1}{dt} = \sigma F(N_0 - \frac{g_0}{g_1}N_1) .$$ (12)

Once the rate equation is defined as shown in Equation (12), the derivation of Beer's law follows by considering the change in incident flux caused by an area of one square meter with thickness *dx* as shown in the figure below, adapted from Bernath.[8]
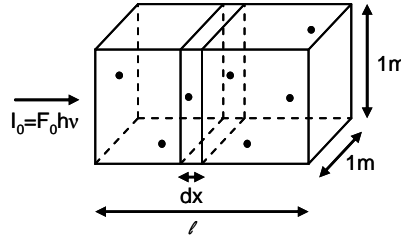
Figure 4. A volume of gas

In this case, the rate of change of flux over the distance *dx* is:

$$dF = -\sigma F(N_0 - \frac{g_0}{g_1}N_1)dx .$$ (13)

The result after integration is:

$$\ln\left(\frac{F}{F_0}\right) = \ln\left(\frac{I}{I_0}\right) = -\sigma(N_0 - \frac{g_0}{g_1}N_1)l ,$$ (14)

where *l* is the path length through the gas, $F = hv/I$, and $F_0 = hv/I_0$. Exponentiation of each side of Equation (14) gives the common form of Beer's law:

$$I = I_0 e^{-\sigma(N_0 - \frac{g_0}{g_1}N_1)l} .$$ (15)

16

Finally, the HITRAN line intensity can be related to the line strength in Equation (7) by the following formula:

$$S' = \frac{2\pi^2 v_{10} S_{10}}{3\varepsilon_0 hcq(T)} e^{-E_0/kT} (1 - e^{-hv_{10}/kT}). \qquad (16)$$

Equation (16) gives the HITRAN line intensity in SI units of m^2-s^{-1}. The HITRAN literature, however, uses units of cm^{-1}/(molecules cm^{-2}). This form is shown below:[9, 11]

$$S' = \frac{8\pi^3 g_0 \widetilde{v}_{10}}{3hcq(T)} e^{-E_0/kT} (1 - e^{-hc\widetilde{v}_{10}/kT}) R_{10} \times 10^{-36}, \qquad (17)$$

where $\widetilde{v}_{10}$ has units of cm^{-1},

$$R_{10} = \frac{S_{10}}{g_0}, \qquad (18)$$

and S_{10} from Equation (7) is given in Debye^2 instead of the SI units of C^2-m^2. Assuming thermodynamic equilibrium, Maxwell-Boltzmann statistics are used to eliminate N_0 and N_1 from Equation (15) with the following relationships:

$$\frac{N_1}{N_0} = \frac{g_1}{g_0} e^{-hv_{10}/kT}$$
$$N_0 = \frac{g_0 N_T e^{-E_0/kT}}{q(T)} \qquad (19)$$

In Equation (19), N_T is the total species concentration in molecules-cm^{-3} and $q(T)$ is the partition function. Using Equation (19) to rewrite Equation (15) results in the form of Beer's law shown here:

$$-\ln\left(\frac{I}{I_0}\right) = \frac{2\pi^2 v_{10} S_{10}}{3\varepsilon_0 hcq(T)} g(v - v_{10}) e^{-E_0/kT} (1 - e^{-hv_{10}/kT}) N_T l. \qquad (20)$$

Using the definition of S' from Equation (17) yields:

17

$$-\ln\left(\frac{I}{I_0}\right) = S' g(v - v_{10}) N_T l . \qquad (21)$$

Integrating over a single absorption line eliminates the line shape function resulting in the final useful form:

$$\int_{-\infty}^{\infty} A(v)dv = \int_{-\infty}^{\infty} -\ln\left(\frac{I}{I_0}\right)dv = S' N_T l = \tilde{\alpha} \cdot l \qquad (22)$$

where $A(v)$ (unitless) is the natural logarithm of the ratio of the intensities of the incident light to exiting light measured by the tunable diode laser along its line of sight and $\tilde{\alpha}$ is the frequency integrated absorption coefficient. If v is reported in wavenumbers, then the integral of A has units of wavenumbers, S' has the HITRAN units of cm^{-1}/(molecules cm^{-2}), N is given in molecules/cm^3, l is given in cm, and $\tilde{\alpha}$ has units of cm^{-2}. A more detailed development stepping from Equation (15) to Equation (22) is given in Appendix A. The plot of $A(v)$ versus v is the absorption spectrum for a laser along a line of sight.[8, 12]

Tunable Diode Laser Absorption Spectroscopy

TDLAS uses a tunable diode laser to measure the absorption of water transitions over a path length. Beer's law can then be used to extract temperature and density from the frequency integrated absorption coefficients of two or more transitions. A tunable diode laser consists of a cavity in a semiconductor material where the intensity is controlled by the input current. As the current to the tunable diode laser is ramped, the change in temperature alters the cavity length of the laser. Thus, current modulation permits the diode to be tuned across a wavelength range. The laser output is sent through the gas of interest and collected on the other side. The natural logarithm of the reference

18

beam divided by the spectrum recorded at the detector gives the absorption spectrum for a line of sight, *A(v)*. Integrating this absorption spectrum over frequency provides the integrated absorption along the path, ∫*A(v)dv*, as seen in Equation (22).

Integrating the absorption spectra from multiple transitions along a single line of sight allows an average temperature to be determined. This was accomplished by scanning three lasers, each in their own wavelength range, to measure multiple absorption features. As discussed at the beginning of the chapter, telecommunications diode lasers were used in this experiment, so the probed wavelength regions (approximately 1391 nm to 1397 nm) fell within the larger wavelength range of the telecommunications diode lasers. Another consideration when choosing the specific nominal wavelength of each diode laser was the term energies (the energy of the initial state) of the transitions found around the nominal wavelength. In thermal equilibrium, the population, and therefore ability to absorb incoming photons, of the initial state of a transition depends on temperature. Thus, if the term energy of a transition is too high to be filled thermally at the temperatures seen in an experiment, the transition will not provide enough absorption to measure with TDLAS. Likewise, if temperatures in an experiment are high, transitions with low term energies may already have a reduced initial state population. Even higher temperatures may not cause a significant reduction in initial state population and therefore the absorption through these regions would not be changed. Thus, transitions were chosen which had initial state populations that produce measurable differences in absorption when they encounter different temperatures in the temperature ranges provided by the experiments.

19

Two methods were used to calculate the temperature from the integrated absorptions. The first method used the data from two transitions to obtain an estimate of the temperature. Using Equation (17), the line intensity at any temperature can be calculated from a given line intensity at a reference temperature using the equation shown below:[11]

$$S'(T) = S'(T_{REF}) \frac{q(T_{REF})}{q(T)} \frac{e^{-E_0/kT}}{e^{-E_0/kT_{REF}}} \frac{1 - e^{-h\nu_{10}/kT}}{1 - e^{-h\nu_{10}/kT_{REF}}} . \qquad (23)$$

Then, using the ratio of two integrated absorptions from Equation (22), the temperature can be calculated as shown here:[12]

$$\frac{\widetilde{\alpha}_1 l}{\widetilde{\alpha}_2 l} = \frac{S'_1 N_T l}{S'_2 N_T l} \approx \frac{S'_1(T_0)}{S'_2(T_0)} e^{[(E_{0_2}/k - E_{0_1}/k)(1/T - 1/T_{REF})]} , \qquad (24)$$

where the subscripts 1 and 2 on all of the variables refer to the transition with which each variable is associated. The ratio of the stimulated emission terms from the two transitions is approximately equal to one, and therefore not included, as shown below:

$$\left(\frac{1 - e^{-h\nu_{10_1}/kT}}{1 - e^{-h\nu_{10_1}/kT_{REF}}} \right) \left(\frac{1 - e^{-h\nu_{10_2}/kT_{REF}}}{1 - e^{-h\nu_{10_2}/kT}} \right) \approx 1. \qquad (25)$$

Equation (24) can then be solved for the temperature, T, using the HITRAN line intensities and measured frequency integrated absorptions.[12] This method can be performed on each line of sight, before tomography, using an analytic two-ring model approach, or after tomography for each individual pixel. Both of these models are discussed further in the TDLAS Burner results section in Chapter IV.

The second method of temperature determination plots two or more integrated absorptions against the term energy of each transition in what is called a Boltzmann plot. Substituting Equation (17) into Equation (22) and rearranging results in:[3, 12]

$$\ln\left[\frac{\int A(\tilde{v})d\tilde{v}}{v_{10}\Re_{10}\times 10^{-36}}\right] = \ln\left[\frac{8\pi^3 N_T l}{3hcq(T)}\right] - \frac{E_0}{kT} + \ln\left[1 - e^{-hc\tilde{v}_{10}/kT}\right]. \qquad (26)$$

The Boltzmann plot is generated by placeing the left hand side of Equation (26) on the ordinate and the term energy, E_0, on the abscissa. Omitting the stimulated emission term, $\ln[1 - e^{-hcv_{10}/kT}]$, causes at most only a few percent error at 2500 K and was therefore generally omitted from the calculation. A linear fit was accomplished for the integrated absorptions where the slope of the fit is equal to $-1/kT$. Again this method was performed analytically for each laser line of sight and pixel by pixel for the absorption tomographic maps. Using the two-zone analytic model, the temperature from the Boltzmann plot agreed with the thermocouple temperature to within 10 K.

Once temperature is determined using either method, Equation (22) can be solved for the total concentration, N_T, where the value of the partition function at T_{REF} and T are given by a piecewise, third degree polynomial fit to HITRAN plots.[9, 13] N_T can also be determined from the y-intercept of the Boltzmann plot using the same method to find the value of the partition function at T.

The pressure can be determined using the Lorentzian contribution to the width of the Voigt profile of the absorption or by substituting $N/V = N_T = P/kT$ from the ideal gas law into Equation (22), where N is the total number of molecules, V is the volume in cm^{-3}, P is the pressure, k is Boltzmann's constant, T is temperature, and N_T is the total species concentration in molecules-cm^{-3}. The pressure broadening term can be determined from the Igor fitting routine used to fit the TDLAS measurements to determine integrated areas. The pressure is then given by:

$$\Delta v_{1/2} = bp, \qquad (27)$$

21

where $\Delta v_{1/2}$ is the full width at half maximum of the Lorentzian contribution to the Voigt line shape and *b* is the pressure broadening coefficient obtained from HITRAN.[8] Pressure determination was not completed for the flat flame burner because pressure within the flame was very close to the pressure in the room. Pressure was calculated for the isolator. Preliminary results are shown in Chapter V.

Tomography

Background

While knowing the frequency integrated absorption coefficient, species density, temperature, or pressure along a given path is valuable information, the line integrals provided by TDLAS measurements do not provide any information about how these values are changing along the path. Spatial variations in temperature and pressure along the path can give important information about the flow. Using tomography, interpolation between the measured beam paths can provide the information necessary to obtain a spatial image of the flow using a limited number of beam paths.[14]

Basis Set Formation

Tomographic reconstruction of the flow characteristics gives much greater insight into the problem. Traditional tomography requires too many lines of sight for situations with limited optical access. Therefore, two models were used to take advantage of *a priori* information in the flat flame burner experiment to reduce the number of beam paths necessary.

The first model used was a two-zone model. This model assumed radial symmetry of the flat flame burner resulting in a hot disk surrounded by room-temperature

22

gas. CFD calculations provided the second model used.[15] The CFD used many of the parameters of the flat flame experiment to determine a radial contour of the gas temperature and density. The CFD models were provided for a range of heights, from 3 mm to 9 mm above the surface of the burner, and scaled with respect to temperature and water concentration to represent various potential operating conditions of the system. Every permutation of height above the burner, maximum temperature, and species concentration was used to generate frequency integrated absorption coefficient maps. The frequency integrated absorption coefficient, $\widetilde{\alpha}$, is:

$$\widetilde{\alpha} = \frac{\int A(v)dv}{l}. \tag{28}$$

The collection of these images covering the range of expected operating conditions for the flat flame burner forms what is called a training set. A more thorough development of the process to create a frequency integrated absorption map from CFD calculations is presented in Appendix B. Example maps are presented in Chapter IV. Many images in the training set provide similar contour information resulting in a great deal of redundancy in the training set. Thus, data reduction techniques can be applied to consolidate the information into a basis set which can then be used to represent the system under investigation. As mentioned in the introduction, two algorithms were applied to the CFD data to obtain the optimal basis set: vector quantization (VQ) and principal components analysis (PCA). The members of the basis set resulting from PCA are orthogonal and can, therefore, be linearly combined to represent any vector in the original training set. Using the optimal basis set and measured absorption data, a two-dimensional temperature, density, or pressure image of the flow can be constructed.[3]

The VQ algorithm was not as useful for basis generation as originally expected. Instead, VQ was used primarily as a clustering and optimization algorithm. It was used to optimize the diameter and center location for the two-zone model of the flat flame burner and the diameter for the CFD model of the flat flame burner. It was also used to find similar shock structure in the time resolved isolator data, allowing averaging of similar shock structures to reduce noise and allow comparison with the isolator CFD.[16]

Although VQ was not used for post-processed tomography, it was used to create the basis functions for the near real-time tomography performed during the isolator experiment. Due to the high degree of redundancy found in the isolator CFD data, images were presorted based on the features contained within them. The isolator CFD data consists of images with very distinct regions. Conditions in the isolator vary from a fairly uniform flow to a shock train when backpressure is added. The flow generally consists of a uniform low pressure area before the shock, the shock front, the shock train, and a trailing area of uniform higher pressure after the shock. The following figure shows an example of the CFD results for the isolator.[3]
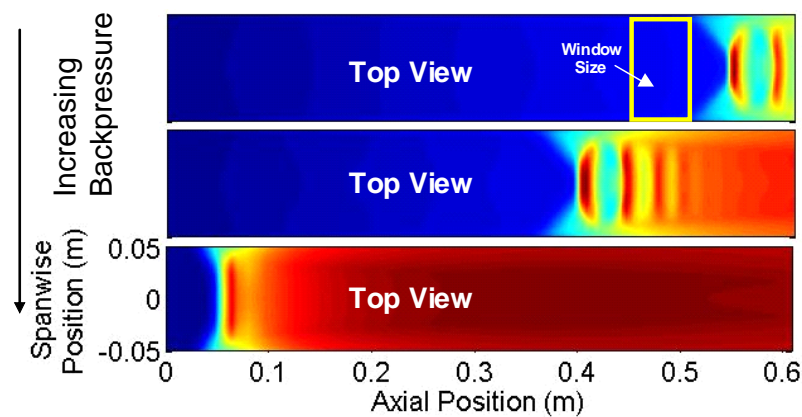
Figure 5. CFD model of frequency integrated absorption coefficient versus position in the isolator as backpressure is increased, blue represents low and red represents high

Note the position of the shock front as backpressure is increased. While the image shows the entire isolator, in reality only a portion of the isolator is probed using TDLAS. As the backpressure was varied, the shock moved through the window where it was measured by TDLAS. A reasonable presort, therefore, of the possible images consisted of a uniform flow to represent the pre and post shock regions and several shapes to represent possible contours of the shock as it passed through the window.

As an initial guess, the first basis set for the isolator was obtained by inspection of the major features in the training set. VQ then took this initial guess as a basis set, classified all of the training set images according to the initial basis set, then averaged over all of the images in each set to create a new basis vector for each classification. The algorithm then proceeded to classify all of the images in the training set according to this new averaged basis set and averaged again. This process continued until the relative change of the new basis set from the previous basis set was within a given threshold. Once the training set was sufficiently classified by VQ, PCA was used on the classified data to produce a basis set for the projection of the TDLAS array.[6] The VQ algorithm can be found in Appendix C in the program Create_VQbasis.

The PCA used for both the near real-time tomography as well as the post-processing tomography was accomplished by first finding the mean of the training set. Once the mean was determined, the projection matrix for the lines of sight from the mean image were calculated and subtracted from the data. The principal components of the training set were then fit to the remaining data. The principal components of the training set were determined by finding the eigenvalues and eigenvectors of the covariance matrix of the training set. The result was a rank ordered set of images where the highest

25

eigenvalue corresponded to the image which captured the highest amount of variance.[5] The basis vectors in each new PCA basis set are orthogonal to each other and can therefore be added or subtracted in linear combinations to reconstruct any image in the training set. The mean image and the first few principal components of the training set became the basis which was used to fit the tunable diode laser data. The PCA algorithm can also be found in Appendix C in the Create_basisv2 program.

Fitting Basis Sets to the Data

Using PCA to perform tomography with the flat flame burner data allowed a comparison with the values obtained from traditional thermocouple measurements. Once a basis set was acquired, the integrated absorptions were fit to a linear combination of the basis set using a least squares fitting algorithm. The projection matrix for each basis image consists of the path integral of each line of sight in the basis image as shown in Figure 6.[14]
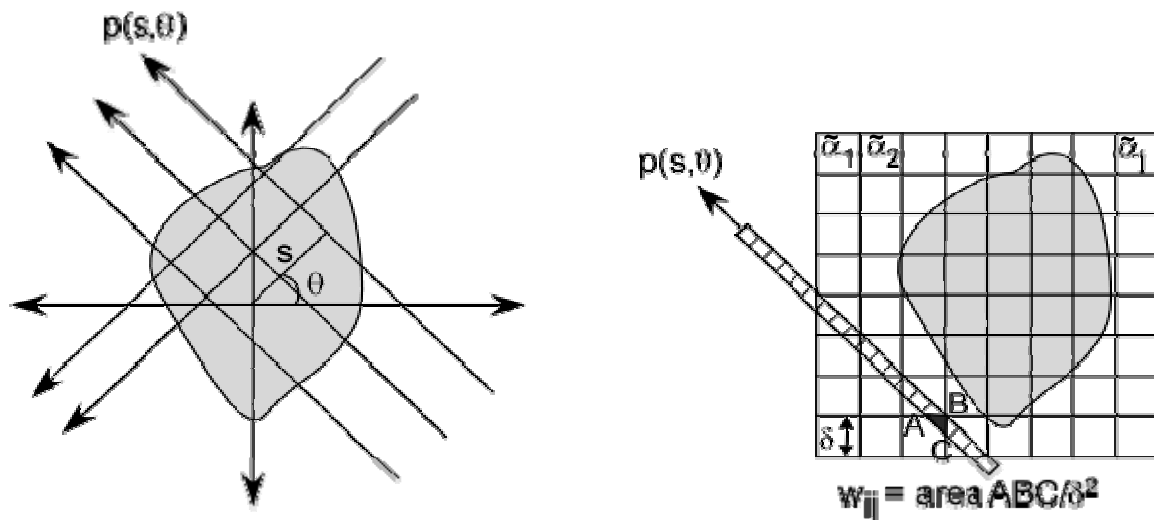
Figure 6. Illustration of path integrals of lines of sight in a basis image

The relation below transforms the path to Cartesian coordinates as a function of θ and perpendicular distance from the origin, s:

$$p(s,\theta)_i = -\int_{-\infty}^{\infty} \ln\left(\frac{I(x,\theta,\nu)}{I_0(s,\theta,\nu)}\right)d\nu = \int_0^L\int_0^L \tilde{\alpha}(x,y)\delta(s-x\cos\theta-y\sin\theta)dxdy = \Re_i\tilde{\alpha} \qquad (29)$$

where $\delta(x)$ is the Dirac delta function, $\Re_i$ is the Radon transform of the ith projection, and ν is the frequency of the TDLAS measurement.[17] Each beam path can then be made discrete by the following equation:

$$\sum_{j=1}^{N} w_{ij}\alpha_j = p_i \qquad (30)$$

where $i = 1,2,\ldots M$ and M is the number of pixels in the reconstructed image. In many applications, such as MRI or CAT scans, a large number of beam paths would be required to obtain, using Equation (30), any sort of spatial resolution. However, using *a priori* information, like the CFD models, assumptions can be made about how contours in the flow will typically look. CFD models produce very large training sets representing all of the possible conditions of the flow. This presents a problem because the number of beam paths required to make the fit well defined increases with the number of images used to perform the fit.[17] The size of the training sets can be reduced, however, using VQ or PCA. The key to reducing the number of beam paths is to expand the absorption function in Equation (30) in terms of a smaller set of basis functions that span the image.[3] By assuming that the absorption at any point in the flow can be approximated by a linear combination of the basis set from the CFD, Equation (29) can be simplified to:

$$\alpha(x,y) \approx \hat{\alpha}(x,y) = \sum_{j=1}^{n} q_j b_j(x,y) \rightarrow p_i = \Re_i\alpha \approx \Re_i\hat{\alpha} = \sum_{j=1}^{n} q_j r_{ij}, \qquad (31)$$

where q_j are the expansion coefficients for α, $b_j(x,y)$ are the basis functions, and r_{ij} is the ith projection of b_j, $\Re_i b_j$. Equation (29) can then be written in the simplified form shown below:

$$\vec{p} = \Re\vec{q} , \qquad\qquad (32)$$

where $\Re$ is the projection matrix with M columns and N rows created by completing M path integrals for N basis functions and $\vec{p}$ is the matrix of line of sight measurements. A least squares approach is then used to solve the matrix equation, determining the expansion coefficient vector, $\vec{q}$. This results in a frequency integrated absorption coefficient map for a single transition.[3]

Finally, once the optimal method for obtaining a basis set from the CFD training set was achieved for the flat flame burner data, the method was applied to the isolator data. Values obtained in the temperature and density maps were compared to thermocouple measurements for the flat flame burner in Chapter IV. Preliminary tomography results using a CFD model for the isolator are shown in Chapter V.

III Thermocouple Flat Flame Burner Results

Introduction

This chapter presents the results of the thermocouple experiment used to determine the temperature profile of a flat flame McKenna type burner. The purpose of this experiment was to provide temperature measurements of the flat flame, obtained using traditional thermocouple measurements, to compare with the temperature results of the TDLAS and tomography detailed in Chapter IV. The first section gives a brief historical background and explanation of the theory of thermocouples. Next, the experimental setup and procedure are discussed in detail. Then, the radiative correction, performed on the thermocouple data due to the high temperatures found in the flame, is discussed. When inside the flame, the thermocouples became hot enough to reradiate a significant amount of energy, causing errors in the thermocouple readings of up to 80 K. A correction was performed to obtain the actual gas temperature in the flame. Finally, the raw and corrected data are presented and discussed.

Background

Thermocouples were originally discovered by Thomas Seebeck in 1821. Every conductive metal generates a potential difference when it is subjected to a thermal gradient. If one end is subjected to a higher temperature than the other, the electrons in the hot end have greater energy and therefore greater velocities. This means they are more likely to be found further from the hot end. Thus, population is increased at the cold end resulting in an electric field and therefore a voltage difference between the two ends. Thermocouples take advantage of this fact by joining two different types of

conductors together at one end and measuring the voltage difference between the two metals at the other end.[18]   Using this method, however, can only provide relative temperature measurements.   Therefore, modern voltage meters contain a calibrated lookup table to determine the actual temperature measured.

Thermocouple Burner Setup

The burner used in this experiment was a flat flame McKenna type burner. The burner consisted of a 60 mm diameter disk of porous bronze through which air and fuel flows. The fuel mixture was controlled by a TYLAN RO-28 meter at 1.31 standard liters per minute (SLPM) of Methane and 15.6 SLPM of Air. This gave an equivalence ratio, or ratio of fuel to air, of 0.8. The equivalence ratio of 0.8 means that the fuel is lean compared to the air, and therefore allows a complete combustion model to be assumed when mole fractions are calculated in Chapter IV. The burner was cooled by a Neslab CFT-25 cooler with a MD-30 pump flowing water at 274 mL/min. Temperature, pressure, and relative humidity in the lab were measured by a NIST traceable Vaisala PTU (pressure, temperature, and humidity) transmitter. Two types of thermocouples were used to measure the temperature profile of the flame. Type B thermocouples, consisting of a platinum-rhodium alloy, have a temperature range of approximately 600 to 2000 K and were used to measure temperatures inside the flame. Type K thermocouples are made of chromel and alumel and have a usable temperature range of approximately 70 to 700 K. Temperatures outside of the flame and up to the boundary of the flame were measured with type K thermocouples.

Three type B thermocouples with bead sizes of 0.33, 0.74, and 1.08 mm were used to measure the temperature of the flame across the center of the burner. The bead

30

size is the diameter of the sphere joining the two thermocouple wires together. The array of type B thermocouples with various bead sizes enabled the radiative correction performed in the next section. The thermocouples were mounted on a translation stage which allowed them to be placed in the center of the burner. The burner was also mounted to a translation stage allowing the thermocouples to scan the entire flame profile. Thin ceramic cylinders were used to stabilize the thermocouples during the experiment. Approximately one quarter inch of each thermocouple was left exposed in the flame to keep the heating of the ceramics from causing any dielectric effect on the thermocouple measurements. A diagram and picture of the type B thermocouple array in the flame is shown below.
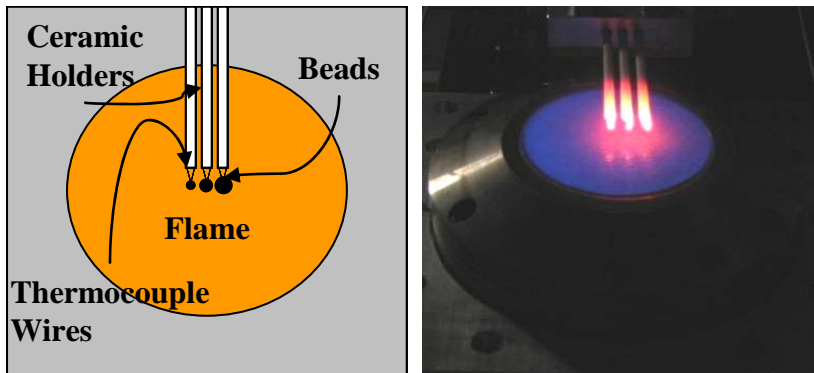
Figure 7. Three type B thermocouples of varying bead diameter placed 6 mm above the surface of the flat flame burner

Two type K thermocouples were used to measure the burner profile from outside the flame at room temperature up to 600 K at the boundary of the flame. Two more type K thermocouples were used to measure the temperature of the input and output water coolant to the burner. This allowed a temperature of combustion to be calculated as shown in the thermocouple results section. Radiative correction was not necessary for the temperatures measured by the type K thermocouples.

Radiative Correction

In the thermocouple flat flame burner experiment, temperatures inside the flame were high enough that the type B thermocouples reradiated a significant amount of energy back into the surrounding environment as shown by the red glow in Figure 7. This lost energy was, therefore, not measured by the thermocouples resulting in erroneously low temperature readings. The amount of energy lost is dependant on the surface area of the bead joining the two wires of the thermocouple. The temperature measurement of the flat flame burner was therefore performed using an array of three type B thermocouples of varying bead diameter. For an object in thermal equilibrium, the heat lost from radiation is equal to the heat gained. In the case of the thermocouples, heat was gained almost completely through convection and lost almost completely through radiation. Using the equation for radiation and Newton's law of cooling, the equation for energy balance on the bead is shown below:[19]

$$
\begin{aligned}
q_{rad} &= \varepsilon A(\sigma_{SB} T_b^4 - \sigma_{SB} T_\infty^4) \\
q_{conv} &= h_{conv} A(T_g - T_b) \\
h_{conv}(T_g - T_b) &= \varepsilon(\sigma_{SB} T_b^4 - \sigma_{SB} T_\infty^4)
\end{aligned}
\qquad . \qquad (33)
$$

In this equation, q_{rad} and q_{conv} are the amounts of heat lost to radiation and convection respectively, ε is the emissivity of the bead, A is the surface area of the bead, σ_{SB} is the Stefan-Boltzmann constant, h_{conv} is the convective heat transfer coefficient between the gas flow and the bead, and T_b, T_g, and T_∞ are the temperatures of the bead, gas and surrounding room respectively. The true temperature of the gas was calculated by rearranging the previous equation into:[19]

32

$$T_b = Cd(m)(T_b^4 - T_\infty^4) + T_g$$
$$\text{where } C = -\frac{\varepsilon \sigma_{SB}}{Nk_{tc}} = -\frac{\varepsilon \sigma_{SB} d(m)}{h_{conv}},$$
(34)

then performing a linear fit to the three data points provided by the small, medium, and large beaded thermocouples. Plotting T_b versus $Cd(m)(T_b^4 - T_{inf}^4)$ gives T_g as the extrapolation to the y-intercept when d goes to zero. In this equation, N is the Nusselt number for the gas and bead, k_{tc} is the gas thermal conductivity, and $d(m)$ is the diameter of the bead. This represents the perfect thermocouple with a bead diameter of zero. A bead diameter of zero has no surface area and therefore cannot radiate.

However, the situation is made more complicated by the Nusselt number's dependence on bead diameter, as shown here:[20]

$$N = 2 + P^{2/5}(0.4R^{1/2} + 0.06R^{2/3})$$
$$R = \frac{\rho_g U}{\mu_v} d(m)$$
(35)

where P is the Prandtl number, R is the Reynolds number, ρ_g is the density of the gas, U is the velocity of the gas, and μ_v is the viscosity of the gas. This additional dependence was included in the emissivity calculation.

At each location where all three thermocouples measured the temperature, data was plotted according to Equation (34); and a linear fit was performed to determine the actual gas temperature. Figure 8 shows an example of this process for three points near the center of the flame; ignoring the dependence of the Nusselt number on bead diameter. For the plot shown here, T_∞ was calculated by averaging the temperatures from six sides of a cube where the bottom of the cube was the surface of the burner and the remaining five sides were the walls and ceiling of the room. The ceiling and surrounding walls

33

were assumed to be 300 K and the surface of the burner was assumed to be 800 K, giving an average of 383 K. The y-intercept gives T_g as 1630 K. As the emissivity and thermal conductivity are constant for the different bead diameters, their values had no effect on the gas temperature.
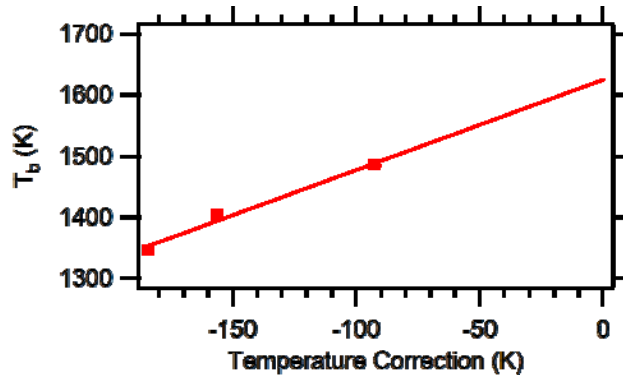
Figure 8. Example of thermocouple correction using Equation (34) with temperatures from the three bead diameters near the center of the flat flame burner

Results

Figure 9 shows the temperature profile for the flat flame burner before the correction was applied. Here the temperature lost due to radiation is readily apparent. The largest diameter bead recorded the lowest temperature due to its larger surface area allowing greater radiation back into the room. The smallest diameter bead recorded the closest to the actual temperature because it is closer to a perfect thermocouple with no surface area and therefore no radiation of heat back into the room.

34
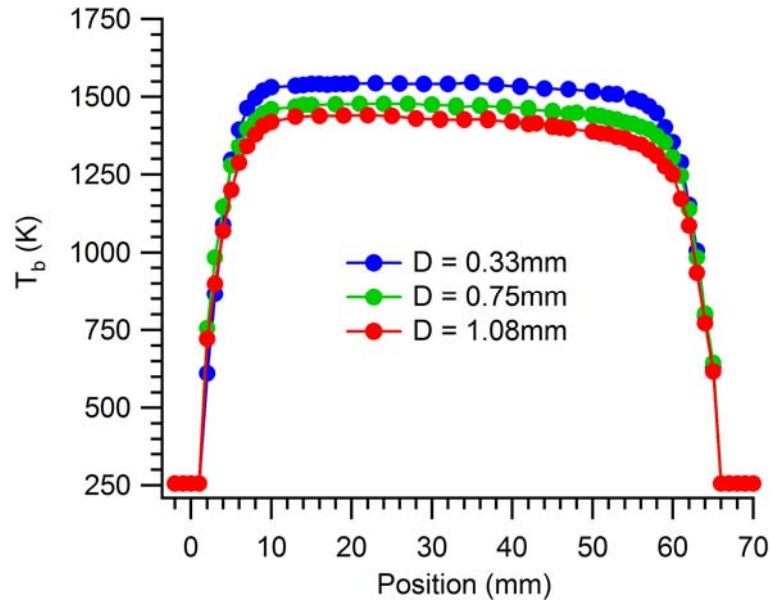
Figure 9. Burner Profile before correction. Note as bead diameter increases, the heat lost through radiation increases and the indicated temperature is decreased

The three thermocouple diameters were measured to be 0.33 ± 0.01 mm, 0.74 ± 0.01 mm, and 1.08 ± 0.01 mm. Using the correction from Equation (34) for a sample three points, the y-intercept in Figure 8 gives the temperature that an ideal point source thermocouple would read. Performing this process across the entire profile and taking the bead diameter dependence of the Nusselt number into account results in the following corrected flat flame burner profile in Figure 10 where the black linear fit comes from the extrapolation of the plot of Equation (34) and the colored lines are the thermocouples corrected independently. The emissivity of the beads was found to be 0.22 which agrees well with previously published results.[21]   Note that the corrected profile gives a temperature of 1638 ± 10 K across the center 40 mm of the burner.
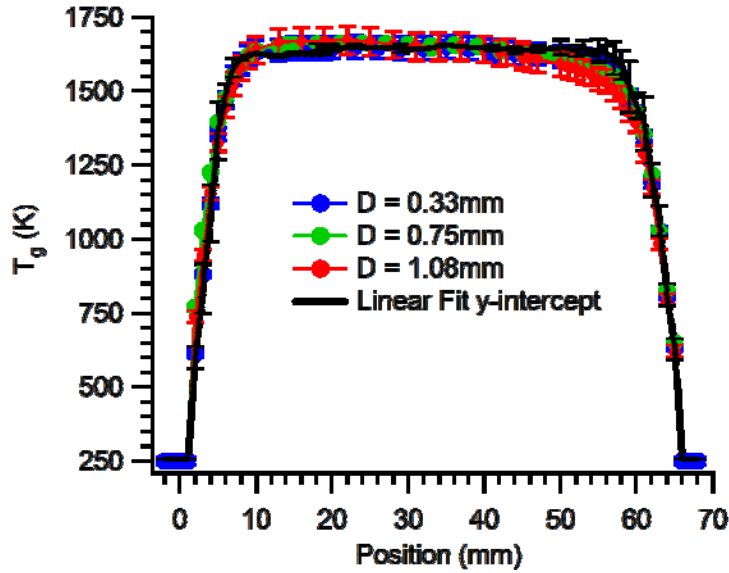
Figure 10. Corrected burner profile showing the corrected profile for each of the three bead sizes and the fit from the y-intercept of Equation (34)

Temperature at the center of the flame can also be obtained using the adiabatic flame temperature of the methane and air mixture. If the adiabatic temperature of the combusting fuel and air mixture is known, then the true flame temperature can be calculated by subtracting the heat lost to the burner. The primary source of heat loss in this experiment was due to the cooling of the flat flame burner with refrigerated water. The input and output temperatures of the water coolant were measured with type K thermocouples. Using the temperature difference between the input and output temperatures of the water coolant along with the heat capacity of water allowed the calculation of the amount of heat lost to the water. For the flow rate of 1.31 SLPM of methane at the equivalence ratio of 0.8 used in this experiment, the adiabatic flame temperature is 1997 ± 50 K.[22] The measured temperature difference of water input to output of 8.16 K, the measured flow of the water of 0.27 L/min, and the specific heat of water of 75.38 J/mol-K give the heat transferred to the burner as 0.15 KJ/sec. The measured flow of methane of 1.31 SLPM and the heat of combustion of methane of 802

KJ/mol give the energy released by the methane as 0.782 KJ/sec. The fraction of energy removed by the water then is given by the ratio of .015 KJ/sec to 0.782 KJ/sec; or 0.19. The adjusted flame temperature is given as (1-0.19) × 1997 K = 1618 ± 50 K for the cooled flat flame burner used in this experiment.[22]

The temperature profile of the flat flame burner obtained through this traditional thermocouple measurement experiment, then further confirmed with a heat of combustion calculation, provides a comparison for the temperatures obtained using TDLAS over a single path and TDLAT with multiple paths in Chapter IV. Also, the flat flame, McKenna type burner was shown to, in fact, be flat in terms of its temperature profile inside of the boundary region. This lends confidence to the symmetry arguments used to create basis functions for tomography in the next chapter. Additionally, the boundary region temperature profile was measured at 1 mm resolution using the thermocouple arrays, which allowed a good evaluation of CFD modeling over this region.

IV Burner TDLAS and Tomography Results

Introduction

The flat flame burner experiment was used as a proof of concept for the isolator experiment. The flow from the flat flame burner is similar to the flow in the isolator in that neither flow is uniform along the line of sight of the laser. Also, methane was used as the fuel for the flat flame burner and as the fuel to vitiate the flow in the isolator. In both cases it provides a controlled amount of water in the flow to be observed using TDLAS. The two experiments are also similar in that, although the flows are not uniform along the lines of sight, they provide planar symmetry. This allows a small array of lasers to provide enough information to achieve two-dimensional tomographic maps of the frequency integrated absorption coefficient, temperature, and water concentration.

This chapter walks through the entire experiment using tunable diode lasers to measure flow characteristics across the flat flame burner. The setup is discussed first, including an in-depth look at the data acquisition system from the function generators controlling the lasers to the detection and conversion of the analog laser intensity to digital measurements. Next, the logic behind the wavelength range chosen for each laser is presented. The third section discusses the process of converting raw intensity data to absorption spectra and integrated absorption. The theory behind the two-zone analytic model as well as the resulting temperature and density determination are presented next. Finally, the tomography section includes the application of the same two-zone model as well as the CFD model of the flat flame burner with a final comparison of all of the methods to the thermocouple experiment results from Chapter III.

TDLAS Burner Setup

TDLAS was performed on the same flat flame McKenna type burner running at the same parameters used in the thermocouple experiment presented in Chapter III. The cylindrical flat flame burner provided a flow with elevated water concentration and temperature in a simplified geometry to be observed by a laser array. Due to the fact that the lines of sight pass through room temperature air on either side of the flame, the flow is not uniform along the path of each laser. Figure 11 shows the schematic of the entire setup.
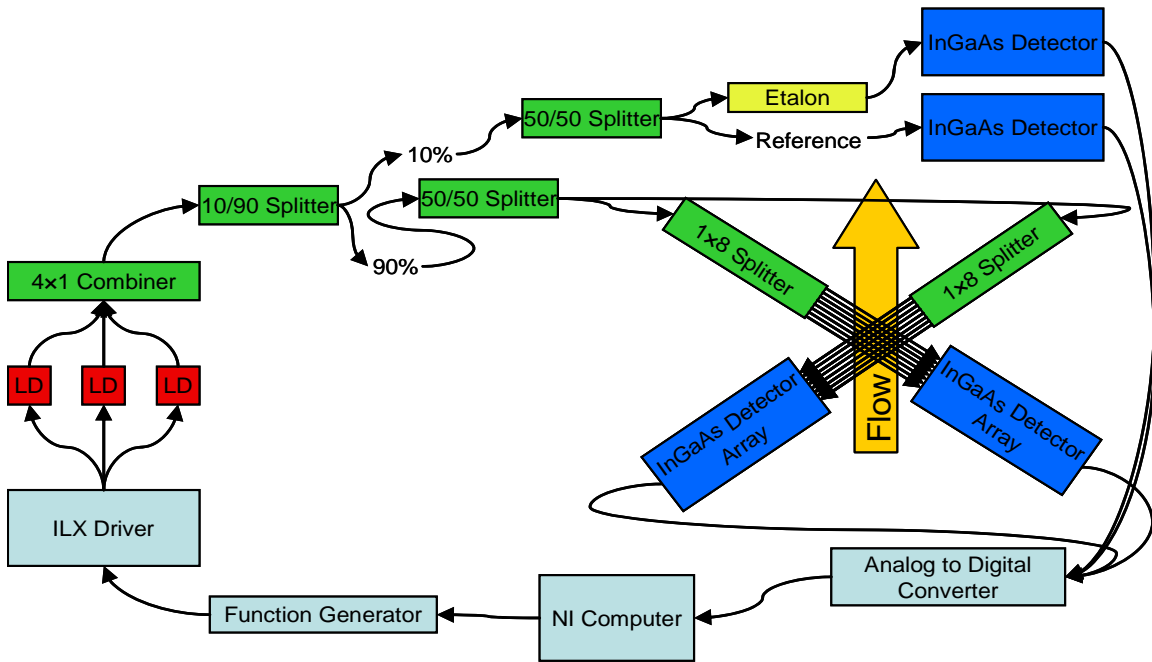
Figure 11. Schematic of optical arrangement for flat-flame burner and isolator experiments

Note that the burner experiment used only one of the tunable diode laser arrays and only seven beam paths. A National Instruments (NI) PXI-8105 computer ran the experimental setup for the flat flame burner and isolator. It sent a control signal to three NI PXI-5402 14-bit, 100 MS/s function generators to provide the current modulation signal to an ILX driver. The ILX driver provided thermo-electric cooling and current to the three lasers.

The three lasers, operating at nominal wavelengths of 1391 nm, 1392 nm, and 1397 nm, were combined into a single fiber by a 4×1 Newport combiner. The combined signal then continued to a 1×2 Newport splitter which sent 10% of the signal to a 50/50 1×2 Newport splitter and the remaining 90% of the signal to another 50/50 splitter. The 50/50 splitter receiving 10% of the signal directed one signal to a SiO_2 etalon for a wavelength measurement while the other was used as a reference beam. The 50/50 splitter receiving 90% of the signal sent each signal to a separate 1×8 splitter. The two 1×8 splitters provided up to 16 beam paths, each containing three wavelength ranges for a total of 48 water absorption spectra. The fibers were coupled to collimators which direct collimated, 1 mm diameter beams through the flame to be recorded on the other side by an in-house designed InGaAs detector array complete with individual preamplifiers. An overhead image of the laser array and detector setup for the flat flame burner experiment is shown in Figure 12.[23] The recorded analog spectra are sent from the board to a NI analog/digital converter before they are sent back to the NI PXI-8105 computer to be recorded into memory.[3] The entire setup enables near real-time data capture and tomography.
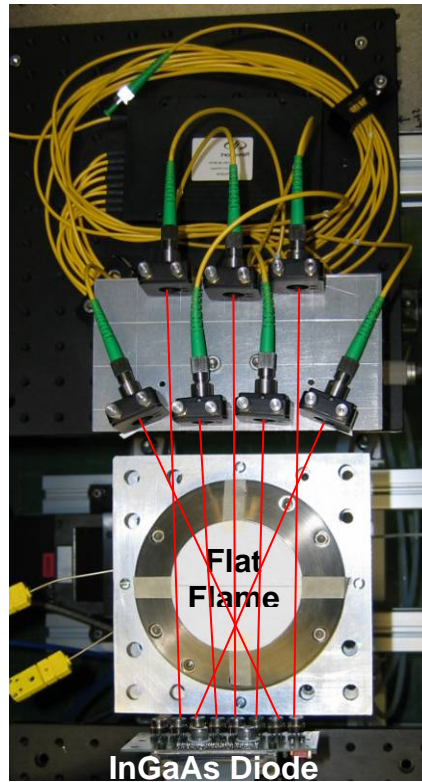
Figure 12. Overhead view of flat flame burner experiment with lines of sight overlaid

Selection of Observed Transitions

Three lasers were used for the flat flame burner experiment. Rough tuning for each of the three lasers was performed using a thermal electric cooler to obtain nominal wavelengths of 1391, 1392, and 1397 nm. This allowed different wavelength ranges, and therefore different transitions of the water molecule, to be observed by each laser. Table 1 and the corresponding graphs in Figure 13 show the identified water transitions in the wavelength regions used.

41

Table 1. The 12 transitions used for experiment are shown in order of increasing wavelength

λ (nm)	v_0 (cm^{-1})	S at 300 K (cm^{-1}-molecule^{-1}-cm^{-2})$\times 10^{-23}$	E_0 (cm^{-1})	v'	$J'\,Ka'\,Kc'$	$J'\,Ka''\,Kc''$	Label
1391.67	7185.60	83.35	1045.06	1 0 1	6 6 0	6 6 1	a
1391.71	7185.40	1.131	1474.98	1 0 1	9 5 4	9 5 5	b
1392.53	7181.16	1488	136.76	1 0 1	2 0 2	3 0 3	c
1392.55	7181.10	7.273	1216.20	1 2 0	7 7 0	7 6 1	d
1392.64	7180.61	3.277	1477.30	1 0 1	9 5 5	9 5 4	e
1392.68	7180.40	55.77	224.84	2 0 0	3 2 1	4 1 4	f
1392.81	7179.75	24.38	1216.20	1 0 1	7 6 2	7 6 1	g
1396.37	7161.41	1168	224.84	1 0 1	3 1 3	4 1 4	h
1396.42	7161.19	.7382	1446.13	0 2 1	11 3 9	10 3 8	i
1396.49	7160.81	.5983	1874.97	1 0 1	10 6 4	10 6 5	j
1396.60	7160.24	421.2	222.05	1 0 1	3 0 3	4 0 4	k
1396.61	7160.19	121.9	173.37	2 0 0	3 0 3	3 1 2	l
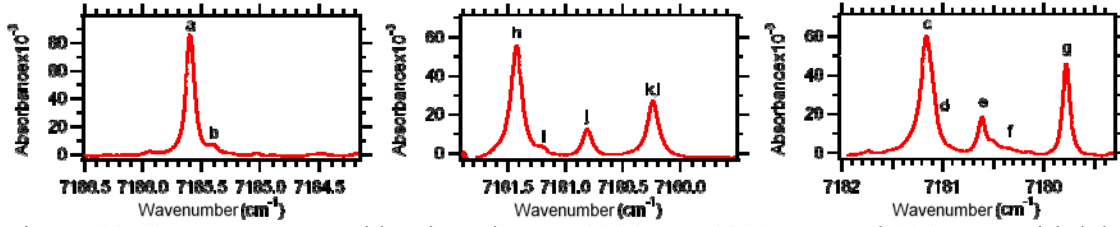
Figure 13. Spectra measured by three lasers: 1391 nm, 1392 nm, and 1397 nm with labels corresponding to Table 1

The selection of these wavelength ranges was based on the specific peaks captured by each laser. Peaks were chosen first based on their intensity, where higher intensity allows them to be integrated more accurately. Second, peaks were chosen to have a range of term energies. This was important to temperature determination because the x-axis of the Boltzmann plots is term energy. Thus, to provide confidence in the linear fit to the Boltzmann plots, a range of initial state energies was required.

Igor Pro was used to perform integrations of all 12 transitions.[7] The fitting routine implements the Humlíček algorithm to obtain a constrained, multi-peak fit.[24] This method provided six data points for the Boltzmann plots resulting in high accuracy temperature calculations. These results are shown in the section covering the two-zone

42

analytic model. Integrating each spectrum individually becomes time consuming when many beam paths are considered. For the number of beam paths necessary to allow accurate tomography, an automated integration routine was developed in Igor. The three peaks with the strongest transitions, and therefore the lowest error for the automated integration, were the 225 cm^{-1}, the 1045 cm^{-1}, and the 1216 cm^{-1} transition. These peaks were used for the tomography results shown later in this chapter. Using fewer peaks results in a less accurate temperature profile, however, so the development of a more rigorous data analysis routine that could fit more peaks automatically would increase the accuracy of the temperature and density results.

From Raw Data to Integrated Absorption

The light intensity observed at the detector is converted into an absorption spectrum, using Equation (22), by taking the natural logarithm of the detected beam divided by the reference beam. Figure 14 shows one millisecond of raw data and the corresponding absorption spectra for each laser.
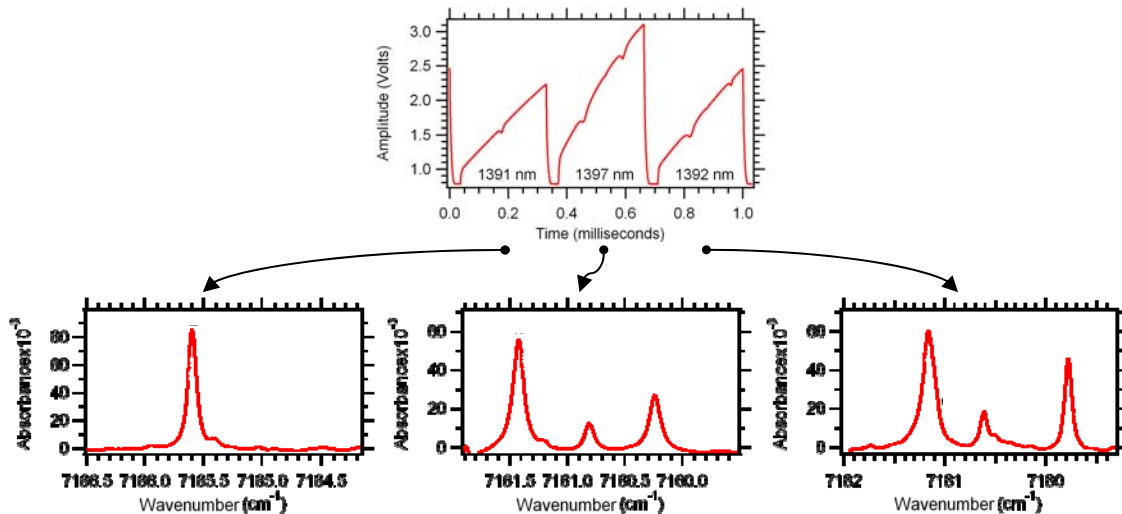
Figure 14. A single period of the raw data from the three multiplexed lasers with the corresponding absorption spectra

43

A multi-peak, baseline Voigt fit was performed using Igor to fit the spectra. The coefficients of the fit were then used to determine the areas of each peak in the spectrum. The results are the frequency integrated peaks, in units of wavenumbers, which are equal to the right hand side of Equation (22). The DAQ software developed to run the flat flame experiments can perform integrations over all of the beam paths, seven for the flat flame burner, of a single selected peak in near real-time.   The seven lines of sight are shown below with the burner in the center position.
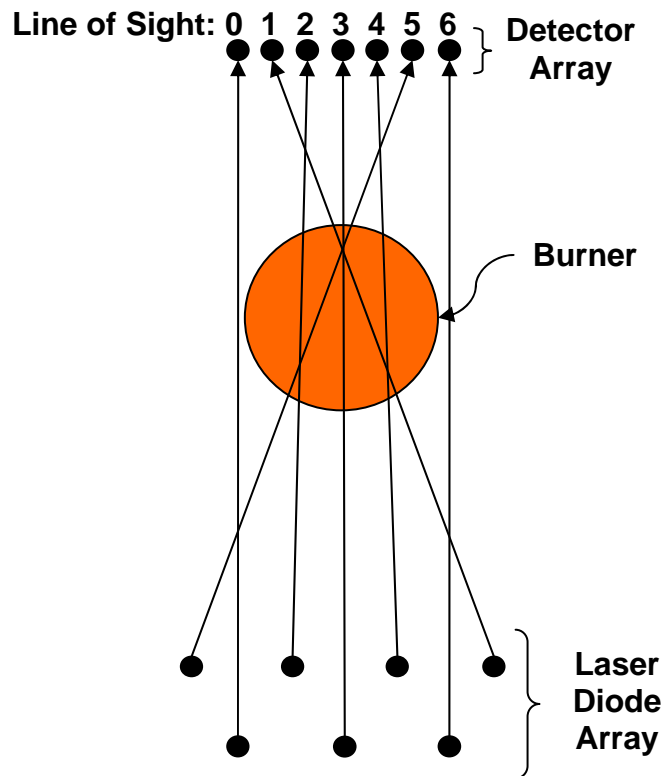
Figure 15. Schematic showing the seven lines of sight used for the flat flame burner experiment

The resulting plots in Figure 16 show the frequency integrated absorption for the 1216 cm^{-1} transition for the seven paths of the flat flame burner experiment with the burner in three positions. As the burner is moved left and right, the profile changes, allowing flame position tracking to within millimeter precision. With only seven beam paths, the

44

information necessary to determine positions and diameter to within millimeters is available. Similar plots will be shown later for the isolator results in Chapter VI.
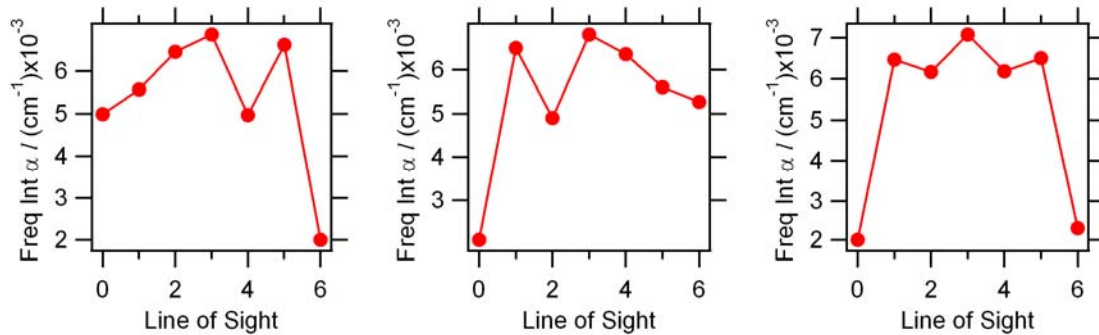
Figure 16. Integrated absorption of the 1216 cm^{-1} transition for each of the seven lines of sight with the flame 9 mm left of center, in the center position, and 9 mm right of center

Two major point of interest are apparent in the graphs in Figure 16: flame position and line of sight path length. First, the 1216 cm^{-1} transition has a smaller initial state population outside of the flames. This is shown in the center graph where both lines of sight, zero and six, are completely outside of the flame. As the flame is shifted left or right, the lines of sight show increased frequency integrated absorption ($\tilde{\alpha}l$) in units of cm^{-1} when the flame moves into their respective paths. Differences in path length can also be extracted from these graphs. Using the center position, in the middle graph in Figure 16 and in the schematic of Figure 15, paths one through five are shown to pass through approximately the same length of hot gas, so the contribution to the intensity from the flame is about the same. Paths one, three, and five, however, show higher intensities than paths two and four. This is due to the longer cold path length of paths one, three, and five. Even though the contribution to the intensity for the 1216 cm^{-1} transition from the cold region is not as great as the contribution from the flame region, the extended path lengths of paths one, three, and five provide enough added absorption that the intensity is noticeably increased. The information available in the graphs of

45

Figure 16, for all three transitions, enables accurate determination of the temperature both inside and outside of the flame, as shown in the next section.

Analytic Two-Zone Model

Before any peaks are integrated, information can be extracted about the burner using a two-zone analytic model by breaking spectra into their constituent hot and cold contributions. Using the assumption that the burner experiment consists of a hot circular region surrounded by room temperature air, a geometric model describing the system can be applied. First, consider a beam passing through a region of room temperature gas followed by a region of hot gas before hitting the detector as shown below in Figure 17.
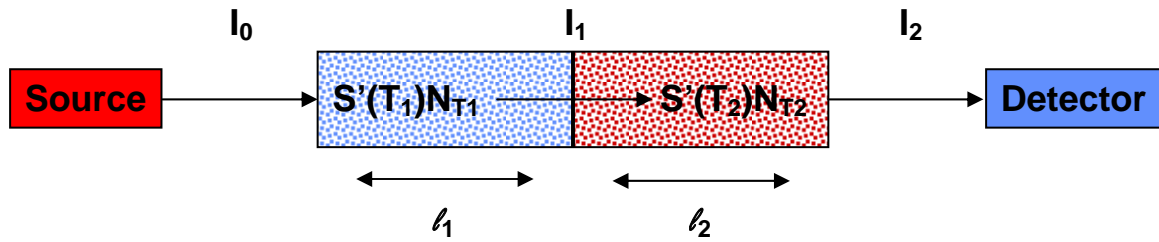
Figure 17. Diagram showing absorption of light through a cold and hot region of gas

The intensity of the incident light after passing through the two regions of gas is governed by Beer's law:

$$I_1 = I_0 e^{-S'(T_1)N_{T_1}l_1g_1(v)}$$
$$I_2 = I_1 e^{-S'(T_2)N_{T_2}l_2g_2(v)}. \tag{36}$$

Substituting in for I_1 for the second region gives:

$$I_2 = I_0 e^{-S'(T_1)N_{T_1}l_1g_1(v)} \cdot e^{-S'(T_2)N_{T_2}l_2g_2(v)} = I_0 e^{-(S'(T_1)N_{T_1}l_1g_1(v)+S'(T_2)N_{T_2}l_2g_2(v))}. \tag{37}$$

Dividing by I_0 and taking the natural logarithm gives:

$$\ln\left(\frac{I_0}{I_2}\right) = S'(T_1)N_{T_1}l_1g_1(v) + S'(T_2)N_{T_2}l_2g_2(v). \tag{38}$$

Now, considering the left hand side of Equation (38) as the total spectrum over the entire path, $ln(I_0/I_2)$ can be labeled as A_T. The two terms on the right hand side of Equation (38) are the contribution to the spectrum from the cold region and the hot region respectively, so $S'(T_1)N_{T1}l_1g_1(v)$ can be labeled as A_C, and $S'(T_2)N_{T2}l_2g_2(v)$ can be labeled as A_H. Dividing A_C by the cold path length, l_1, and A_H by the hot path length, l_2, then gives the cold and hot spectra per unit length. Using the beam geometry shown in Figure 18, the outside beam paths can be averaged and divided by the path length to give A_C/l_1. To find A_H/l_2, however, the diameter must first be determined. Once these spectra per unit length are determined, they can then be used as reference spectra and multiplied by the lengths of the hot and cold spectra of any beam path to reconstruct the total spectrum as:

$$A_T = A_C \frac{(L-d)}{L_C} + A_H \frac{d}{D}, \qquad (39)$$

where L_C is the path length of the cold reference spectra, previously called l_1, D is the diameter of the flame, L is the path length of the line of sight under investigation, and d is the path length of the line of sight through the flame, previously called l_2. The change of variables allows the diameter to be calculated using a cold reference path, with no hot contribution, and two paths with different lengths of hot contribution.[14, 17] The setup described here is shown in Figure 18.
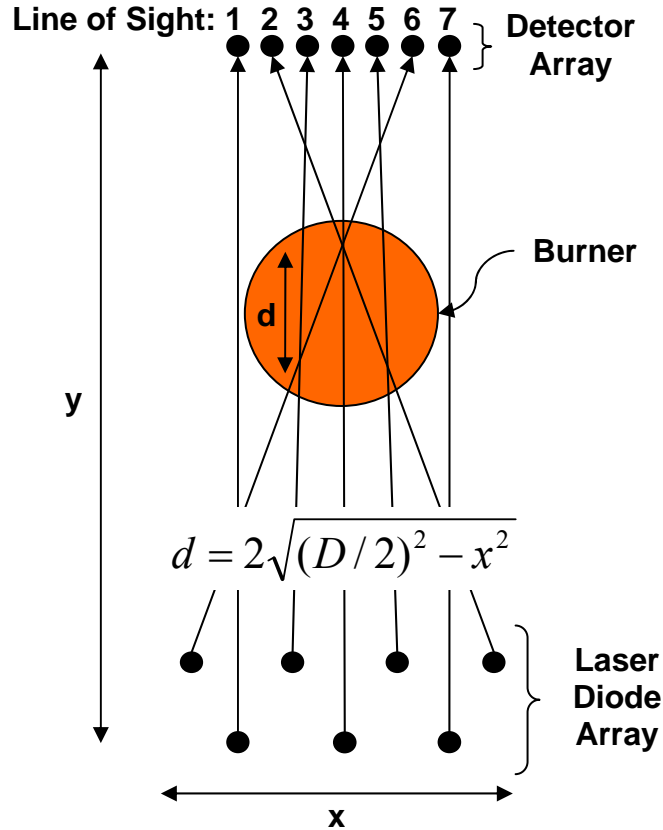
Figure 18. Diagram of burner with line of sight overlay

The diameter is determined by solving for A_H of two paths with different path lengths through the flame, d, and setting them equal to each other. The result after some algebra is:

$$\frac{d'}{d} = \frac{A_T' - A_C L'}{A_T - A_C L}. \tag{40}$$

Rearranging Equation (40) enables the solver in Microsoft Excel to determine the ratio of d'/d which minimizes the following equation:

$$\left(A_T' - A_C L' \right) - \frac{d'}{d}\left(A_T - A_C L \right) = 0. \tag{41}$$

The diameter can then be determined using geometry, where

48

$$\frac{d'}{d} = \frac{2\sqrt{(D/2)^2 - x'^2}}{2\sqrt{(D/2)^2 - x^2}}. \qquad (42)$$

Once D is known, the cold contribution to the center path length can be subtracted off, leaving a reference hot spectrum, A_H. With the reference spectra A_C and A_H and their corresponding lengths L_C and D determined, all of the lines of sight can be split into their hot and cold spectrum contributions. This allows for more accurate integration of the absorption spectra which enables very accurate path length, and temperature determination.

Because the initial level populations for each transition are dependent on temperature, they give different diameters of the flame. For example, due to its lower term energy, the initial state of the 1045 cm^{-1} transition (in the 1391 nm spectrum) begins to fill thermally before the initial state of the 1216 cm^{-1} transition (in the 1392 spectrum). Thus, as the line of sight moves closer to the edge of the burner and temperature increases, the frequency integrated absorption coefficient for the 1045 cm^{-1} transition becomes larger before the frequency integrated absorption coefficient for the 1216 cm^{-1} transition. The result is a larger diameter determination when using the 1045 cm^{-1} transition. The diameter results for each spectrum are shown in Table 2.

Table 2. Results of diameter determination using two-zone analytical method

TDL Center Wavelength (nm):	1391	1392	1397
Corresponding Transition (cm^{-1}):	1045	1216	224
Diameter (mm):	66.9	62.0	56.9

With separate hot and cold spectra, the integrations of the various lines can be performed very accurately. Using the separated hot and cold spectra, where the diameter of the flame was determined with the 1397 nm spectrum, Boltzmann plots were created for the hot and cold region, as shown in Figure 19.

49
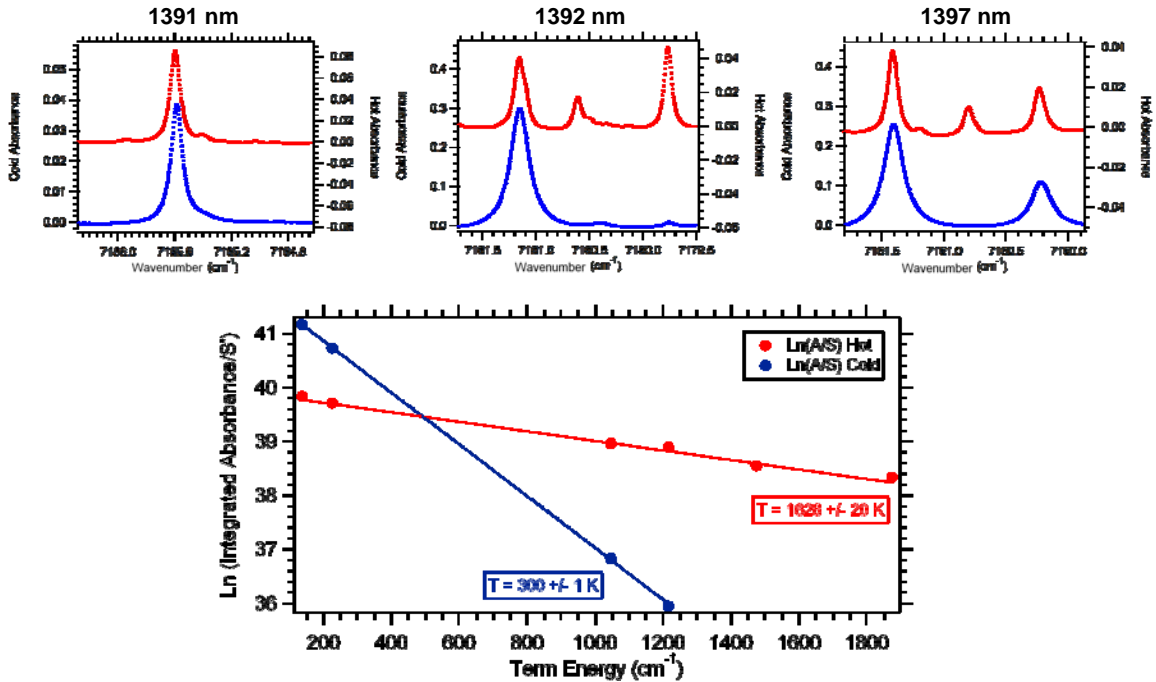
Figure 19. Separated spectra and Boltzmann plots resulting from peak integrations

The resultant temperatures and calculated mole fractions compare extremely well with the thermocouple measurements as shown in Table 3. In the table, the 40 and 58 mm averages refer to the length across the flame used to calculate an average temperature. For example, the 40 mm average uses the center 40 mm of the temperature profile shown in Figure 10, from approximately 14 mm to 54 mm. Note the mole fraction for the 40 mm average of the hot region, 0.1547, comes from a model assuming complete combustion.[22] This number was not available for the 58 mm average of the thermocouple data which includes some of the boundary layer.

Table 3. TDLAS Temperature and mole fraction results and comparison to thermocouple measurements and calculated mole fractions.

Measurement	Temperature (K)	Mole Fraction
TDLAS Hot	1628 ± 20	0.157±0.008
TC Hot (58 mm average)	1583 ± 124	N/A
TC Hot (40 mm average)	1638 ± 10	0.1547
TDLAS Cold	300 ± 1	0.0071±0.0004
TC Cold (at 15 mm from flame)	302 ± 2	0.0061±0.0004

50

The results from the section are obtained using a completely analytical approach to perform tomography. In a flow where conditions are changing, like that of a scramjet, many more datasets would need to be acquired, resulting in more data and necessitating a computational approach to perform tomography. This same two-zone model can still be used in a computational approach, as shown in the next section.

Computational Tomography

Tomography for the flat flame burner was performed using two models for basis set generation. The first method uses the same basis set as the analytical two-zone model where a radially symmetric hot center region is surrounded by cooler, room-temperature gas. It uses beam paths outside of the flame to define the cold region, and then performs a fit to capture the flame region. The second model uses a radial temperature and density profile from CFD. This model provides contour information in the boundary region, which the two-zone method cannot capture.

Two-zone Model

The two-zone model is a very basic example of the use of a basis created from *a priori* knowledge to reduce the number of lines of sight necessary to perform tomography. It uses the same symmetry arguments as the two-zone analytic model and therefore provides an excellent comparison. The three transitions with the smallest integration error were used for the tomography portion of the experiment: the 225 cm^{-1}, 1045 cm^{-1}, and 1216 cm^{-1} transition. For each transition, an absorption coefficient map was calculated by first constraining the cold region using only the beam paths outside of the flame, then fitting the hot region separately. See the Tophatfixedcold program in

51

Appendix C for the actual code. To fit the data to the hot region, the projection matrix for the beams in the cold region was used to determine the amount of integrated absorption that contributed to each line of sight due to the cold region. These path integrals were then subtracted from the integrated absorption given by the detectors. The remaining absorption was then due completely to the hot region which was fit independently. The independent hot region fit was done by making an absorption map where the hot region was set to one and the cold region was set to zero as shown in Figure 20. The adjusted data were fit to the hot basis map by scaling it with a coefficient. The fitted integrated absorption map was the result of the fixed cold basis map added to the scaled hot basis map.
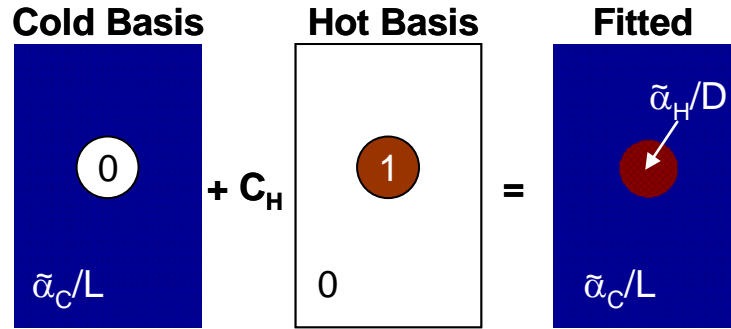
Figure 20. Basis images and resultant fit absorption map

The automation of the fitting process lends itself to an optimization where the flame diameter and the center location of the basis set are varied. The residual of the fit, as these parameters are varied, shows how well the basis model matches the data collected at the detectors using the following equation:[3, 16]

$$Residual = \sum_{i=1}^{\#LOS} abs[\tilde{\alpha}_i L_i - C * p_i], \qquad (43)$$

where $\tilde{\alpha}_i$ is the frequency integrated absorption coefficient from the ith beam path, L_i is the length of the ith beam path, C is the fit coefficient of the basis image, and p_i is the line

52

integral along i^{th} beam path in the basis image. Using this logic, the minimum values of the residual maps were used to determine where the best fit occurred. The diameter determined using the optimization technique matches up well to the measured flame diameter, as well as the diameter given by the two-zone analytic model.
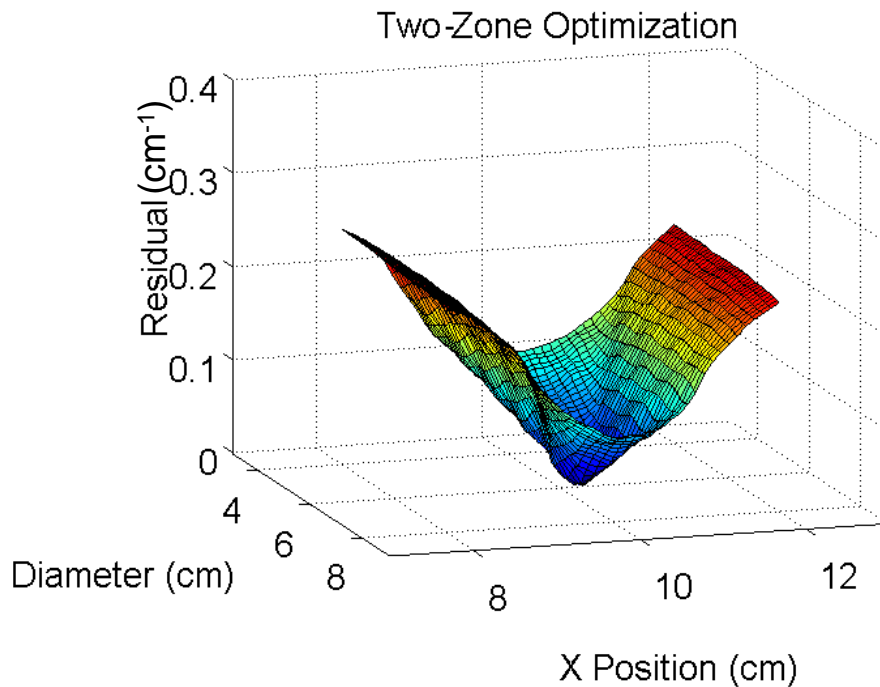
Figure 21. Two-zone optimization showing residual as a function of x position of the center of the burner and the flame diameter are varied

The plot in Figure 21 used 63 lines of sight, so both diameter and x position are well defined resulting in a large curvature at the minimum. Table 4 shows the measured diameter of the porous surface of the flat flame burner as well as the analytic two-zone model solution for the diameter using each of the three transitions. Table 5 shows the results of all of the different combinations of transitions and number of beams used. All of the residual based center x position results agree with the measured center of 10 cm to within 0.3 cm. The diameter results agree with the physical diameter of the burner to within 0.5 cm. Also note the correlation between the analytic method diameters and the

53

tomography residual diameters for each transition. Due to their sensitivities at different temperatures, each of the transitions begins to pick up the boundary layer at different points. Both methods show the 225 cm^{-1} transition obtaining the smallest diameter of 5.7 ± 0.2 cm. The next largest diameter determination comes from the 1216 cm^{-1} transition, with both methods giving 6.1 ± 0.3 cm. The 1045 cm^{-1} transition gave the largest diameter of 6.4 ± 0.2 cm.

Table 4. Measured and calculated flame diameters from physical apparatus and two-zone analytic model

Transition (cm^{-1}):	225	1045	1216
Physical Diameter of burner (cm):	6.0		
Analytic Diameter (cm):	5.7	6.7	6.2

Table 5. Results of two-zone optimization of the x position of the center of the burner and the diameter of the flame

Transition (cm^{-1})	Beams Used	X Position (cm)	Diameter (cm)
225	7	10.3	5.8
	63	10.2	5.5
	119	10.2	5.5
1045	7	10.0	6.5
	63	10.0	6.5
	119	10.0	6.5
1216	7	10.1	5.8
	63	10.1	6.3
	119	10.1	6.3

Due to the large number of beam paths crossing the x direction, as shown in Figure 18, there is enough information to provide a good estimate of the center position. In the y direction, however, information is provided only by the diagonal beam paths. The surface plot of the two-zone residual map as both the x and y center positions are varied as shown in Figure 22.
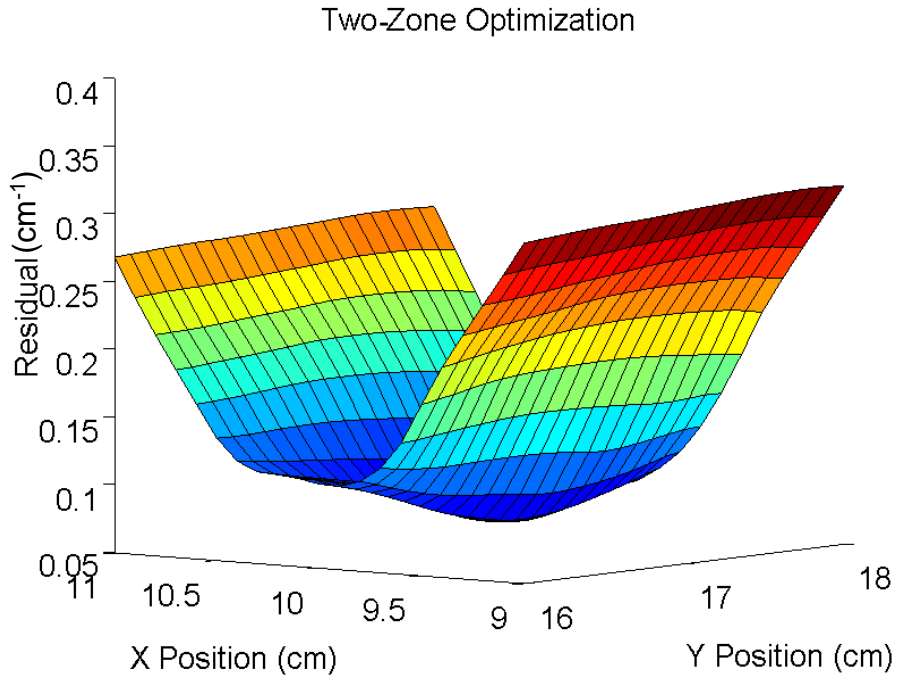
Figure 22. Two-zone optimization of the x and y position of the center of the burner using tomography

While the curvature at the minimum of the residual map in the y direction is not as large as the x direction, a clear minimum is still discerned. Table 6 shows the results of each of the transitions with three different numbers of path lengths. Even with the limited information in the y direction, the center y position is located to within 1 cm of the measured position of 16.7 cm.

Table 6. Results of tomography optimization to find the center position of the flame

Transition (cm^{-1})	Beams Used	X Position (cm)	Y Position (cm)
Measured	-	10.0	16.7
225	7	10.4	17.1
	63	10.2	16.3
	119	10.2	16.4
1045	7	10.0	16.7
	63	10.1	17.4
	119	10.0	17.3
1216	7	10.1	16.4
	63	10.1	17.3
	119	10.1	17.1

Once a fitted integrated absorption map was completed for each of the three transitions, a Boltzmann plot was then constructed pixel by pixel. From the temperature plot, a water density was calculated. The temperature and density surface plots using the optimized diameter from the 1216 cm^{-1} line of 6.3 cm are shown here in Figure 23. A comparison to the thermocouple results and CFD tomography results is shown at the end of the next section.
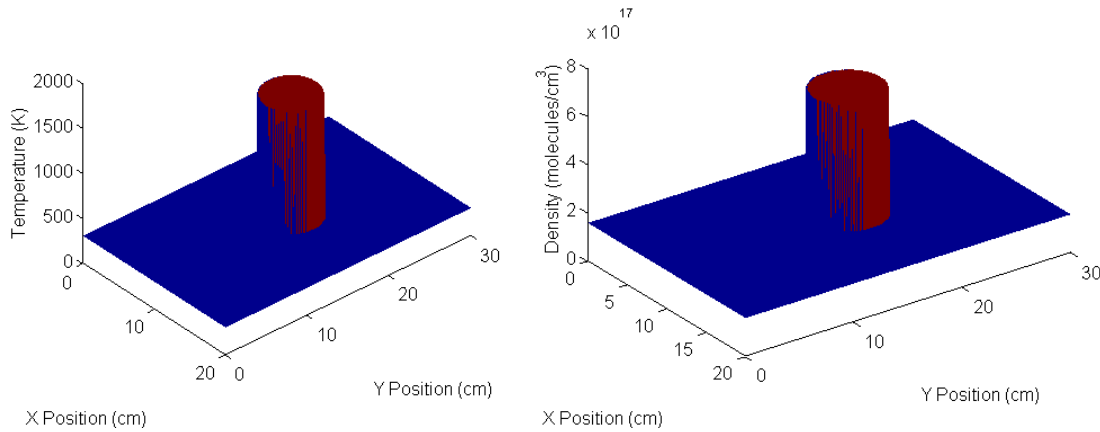
Figure 23. Temperature and density maps using tomography with the two-zone model basis images

CFD Model

The CFD calculations provide the temperature and density as a function of distance from the center of the flame at varying heights above the burner surface. Radial symmetry was assumed to create temperature and density maps. The radius was scaled using an optimization technique similar to that used in the two-zone model. See the program Bestratio in Appendix C for the actual algorithm. The radial plots of the CFD calculations are shown in Figure 24. Again, note the difference in sensitivity of the three transitions to the boundary layer. These differences result in the different diameter

determinations of both the two-zone analytical model as well as the two-zone optimization.
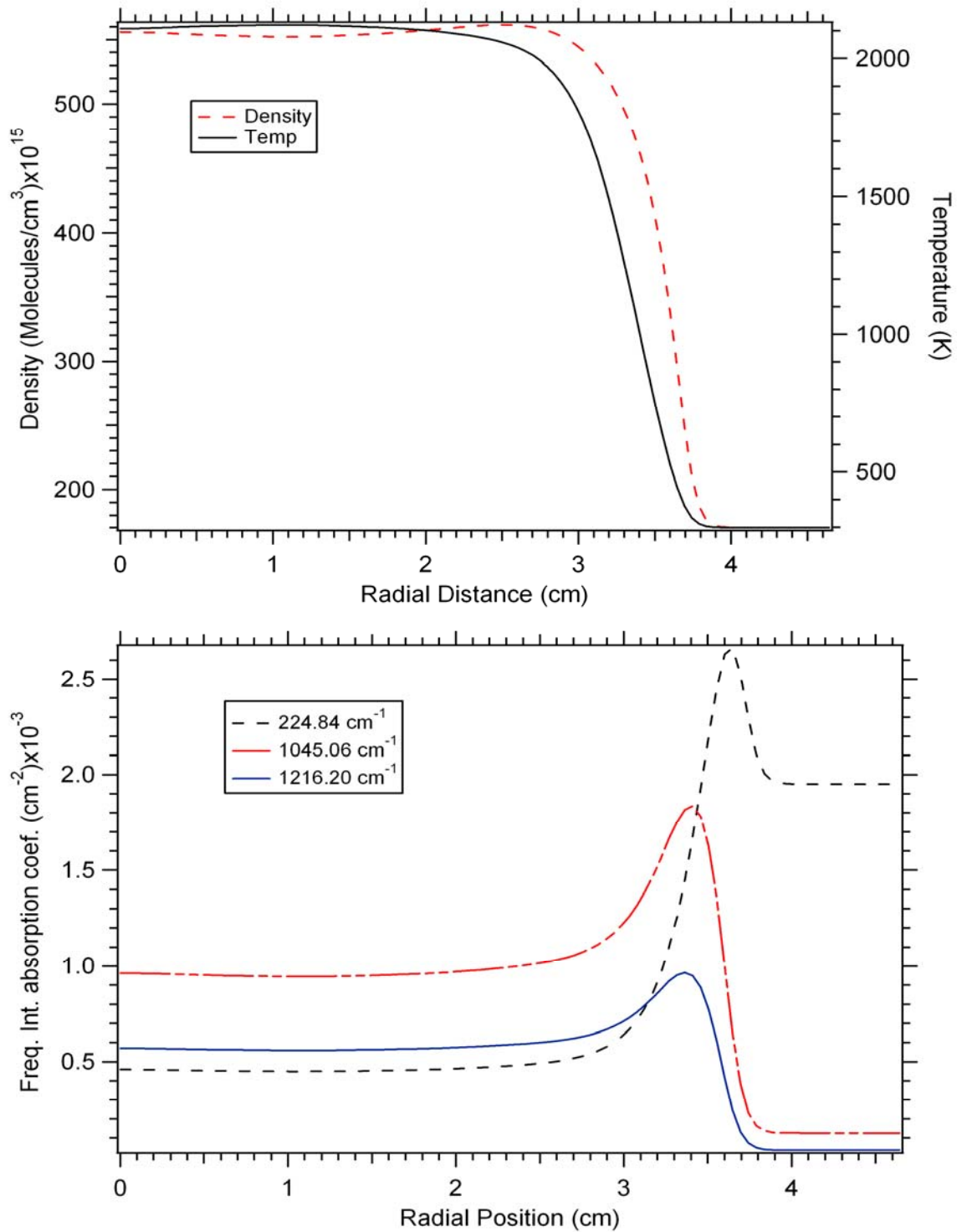
Figure 24. Radial temperature and density from CFD calculations and the resulting radial absorptions for the three transitions used for tomography

The results of the radius optimization are shown in Figure 25. A fit residual was calculated for each of the three transitions over a range of scaled radii of the CFD from 0.75 to 1.25 in increments of 0.01. The range over which a good fit to the basis functions can be obtained is different for each transition. Also, the residuals are fairly flat for a range of values in which a good fit can be achieved by scaling the diameter and temperature of the flame. Essentially, a basis image with a smaller flame diameter can still maintain the same line integral to fit the data as long as the temperature of the flame is increased at the same time. However, once the diameter becomes so large that it pushes into the path of a line of sight that is showing no flame contribution, the residual rises dramatically. Conversely, if the diameter becomes so small that a line of sight which does show flame contribution is left outside of the flame, the residual quickly increases again. To overcome these difficulties, a weighted average of the best fit radius was performed by adding the inverse of the three individual residual plots. This method weights the residual plots with the lowest residual, and therefore best fit, the highest. The result is shown by the black line trace in Figure 25. The maximum of the weighted sum of the inverse residuals is achieved at a value of 0.9. This indicated that the x-axis of the radial temperature and density profiles given by the CFD calculations needed to be scaled by a factor of 0.9 to fit the TDLAS data.

58
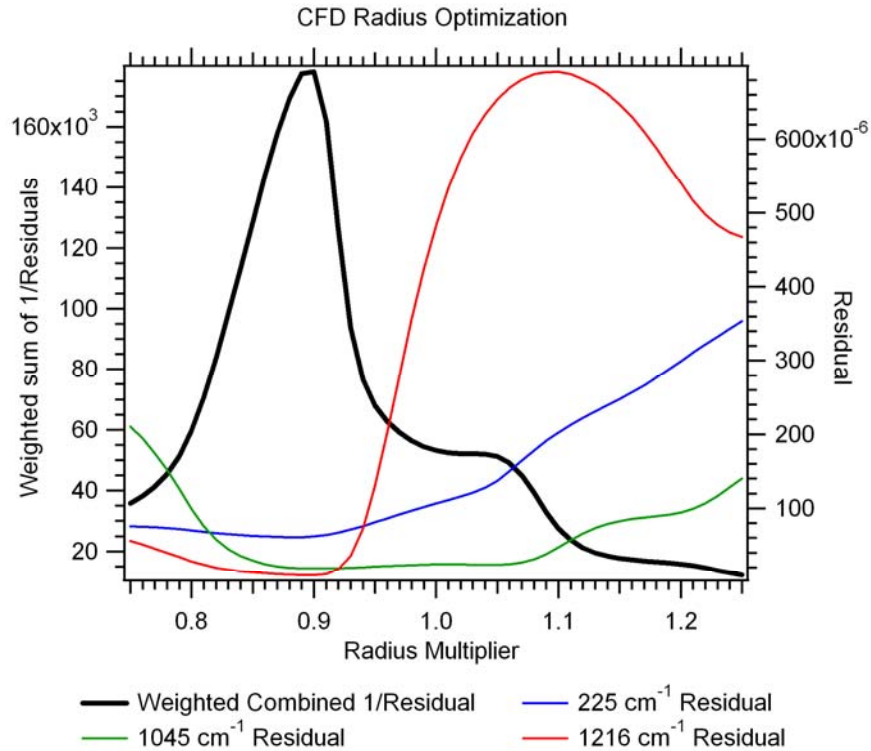
Figure 25. Residuals and combined weighted inverse of residuals showing the
optimization of the radius of the CFD training set

The training set was constructed using the CFD calculations over a range of heights from 3 mm to 9 mm above the surface of the burner. Each of the heights was then scaled to a maximum temperature and a peak density to minimum density ratio. The resulting training set consisted of 175 integrated absorption maps which capture a wide range of possible conditions of the burner. Using all 175 snapshots to fit the data for each line, however, would make the fit underdetermined unless more lines of sight were added. To achieve a well-posed problem, principal component analysis was used to reduce the dimensionality of the training set and thereby reduce the number of lines of sight necessary.

The first step of the PCA algorithm fit the data to the mean of the training set. Then, the projection matrix from the mean image was subtracted from the data like the

59

two-zone model where the fixed cold contribution was subtracted from the data. The remaining integrated absorption coefficient for each path was fit to a linear combination of a justified number of the first principal components.

The justification for the number of principal components used was provided by the representation error and the condition number. The representation error is a percentage error that describes how well, on average, each image in the training set can be constructed as a function of the number of principal components kept to do the reconstruction. See Reperr2 in Appendix C for the algorithm. For complex distributions, keeping more images in the basis set allows better representation of every image in the training set. The condition number can be thought of as an error multiplier. The error in the measured data will be greater in the fit coefficients by a factor of approximately the condition number. Condition numbers around 10 or less were used to define a well posed mathematical problem for this experiment.

Table 7. Condition number under varying conditions

	E_0 (cm^{-1})	7 Beampaths	63 Beampaths	119 Beampaths
3 BASIS VECTORS	225	148	100	40
	1045	528	26	10
	1216	324	13	7
2 BASIS VECTORS	225	31	16	12
	1045	9	4	4
	1216	4	4	5
1 BASIS VECTOR	225	1	1	1
	1045	1	1	1
	1216	1	1	1

Table 8. Average representation percent error for the three transitions using varying numbers of principal components

	225 cm^{-1}	1045 cm^{-1}	1216 cm^{-1}
3 BASIS VECTORS	.03 %	.13 %	.20 %
2 BASIS VECTORS	.18 %	.25 %	.34 %
1 BASIS VECTORS	.46 %	8.34 %	17.20 %

As shown in Table 7, using more lines of sight lowers the condition number because additional information is available to constrain the fit. Table 8 shows that the representation error is under one percent when two principal components are retained. Using the information of Table 7 and Table 8 together, keeping two principal components with 119 beam paths was chosen as the optimum solution. Figure 26 shows the mean and first two principal components for the 1216 cm^{-1} transition. The linear combination of these three images results in the fit absorption map.
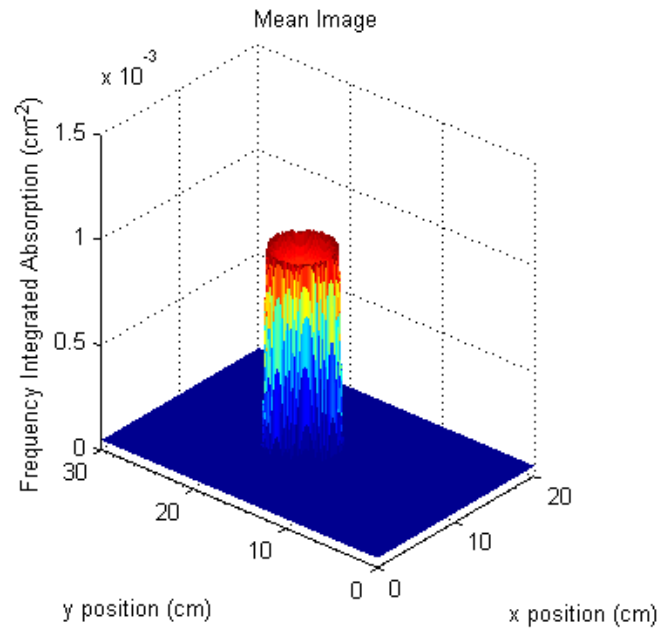
Figure 26.a. The mean image of the training set for the 1216 cm^{-1} transition
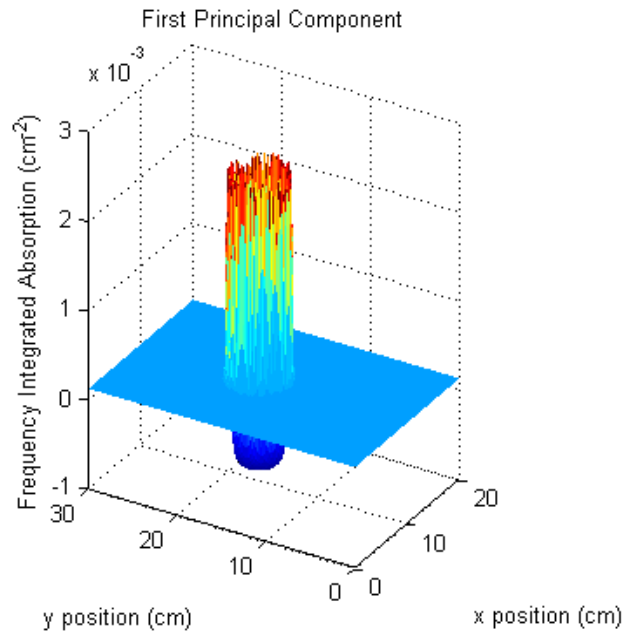
Figure 26.b. The first principal component for the 1216 cm^{-1} transition
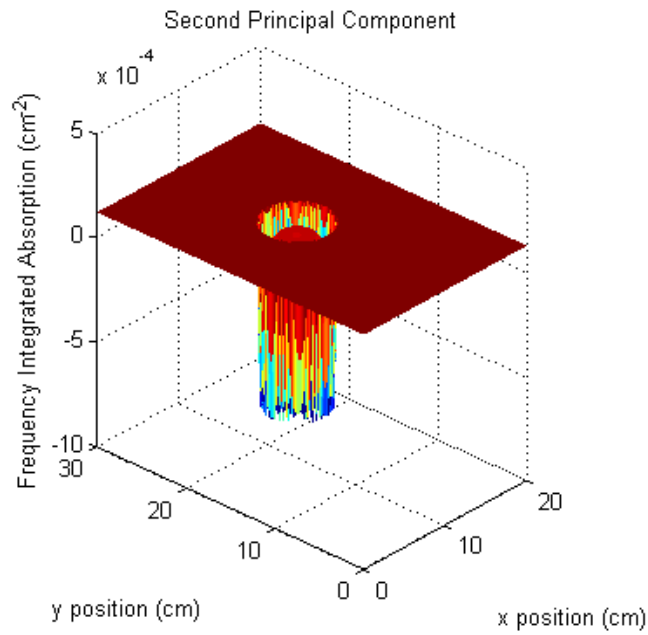
Figure 26.c. The second principal component for the 1216 cm^{-1} transition

62
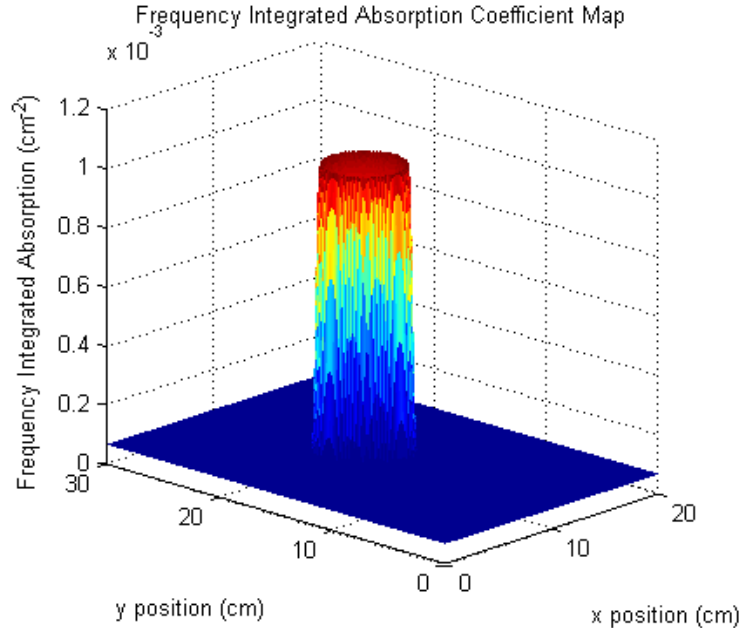
Figure 26.d. Fit absorption map for the 1216 cm^{-1} transition

Figure 26. Fit coefficients for the mean image and first two principal components are multiplied by their corresponding basis image then added in linear combination to produce the fitted frequency integrated absorption coefficient map

Like the two-zone model, temperatures were calculated pixel by pixel using the three fitted integrated absorption maps while density was calculated from the temperature map using Equation (18). Figure 27 shows the absorption maps using 119 beam paths and two principal components for the three transitions under investigation. Again, the different temperature sensitivities are readily apparent in the absorption maps. Due to the low ground state energy of the 225 cm^{-1} transition, the population of the initial state decreases in the flame due to thermal excitation. This causes the absorption to decrease in the flame resulting in an absorption map with a "bowl" in the center. The thermal excitation from the flame increases the initial state populations of the 1045 cm^{-1} and 1216 cm^{-1} transitions resulting in top-hat shaped absorption maps shown here.

63
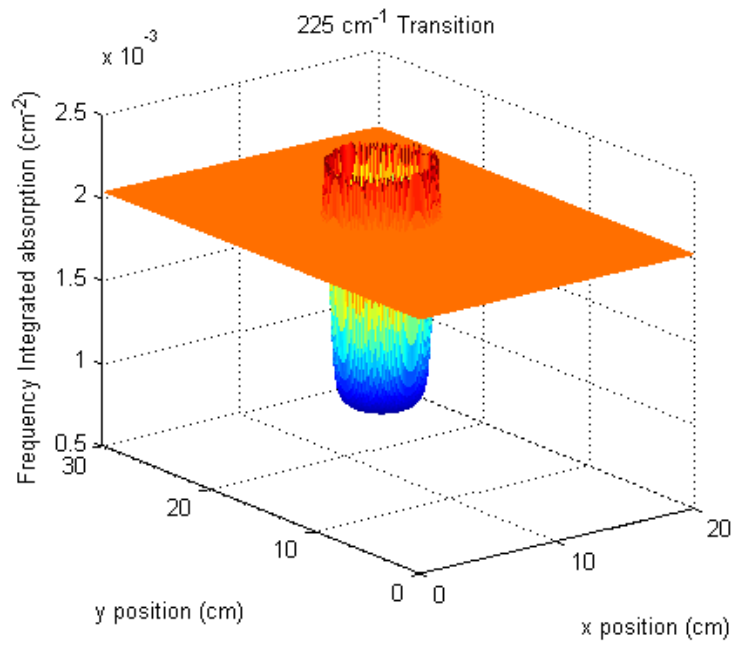
Figure 27.a. Fit absorption map for the 225 cm^{-1} transition
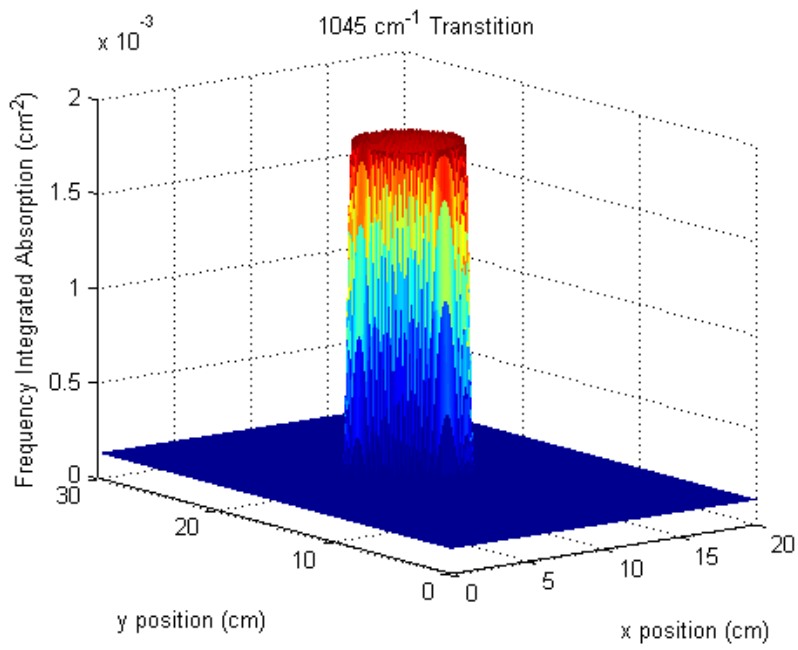
Figure 27.b. Fit absorption map for the 1045 cm^{-1} transition

64
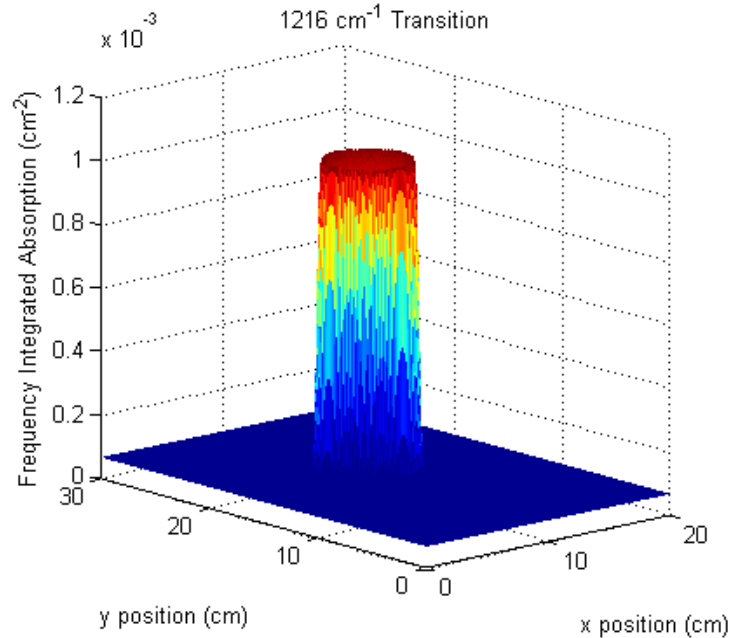
Figure 27.c. Fit absorption map for the 1216 cm^{-1} transition

Figure 27. Example frequency integrated absorption coefficient maps for each of the three transitions of interest

Combining the information from the three absorption maps using a Boltzmann plot at each pixel results in the temperature map shown in Figure 28. Again, solving Equation (22) for N_T results in the water density map shown in Figure 28. Using the scaled CFD images as a basis for the lines of sight allows accurate profile determination for the flat flame burner.
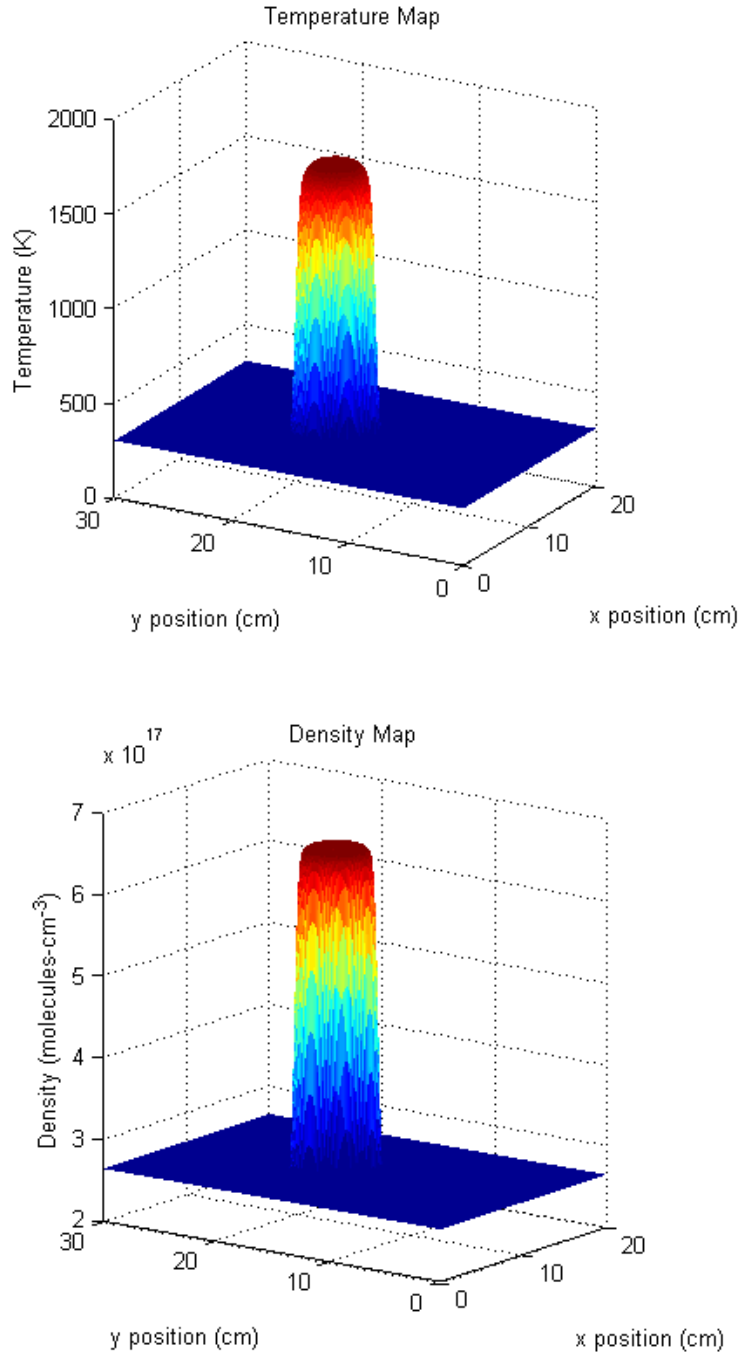
Figure 28. Composite temperature and density contour plots for the flat flame burner using the first two principal components and 119 beam paths

Taking a slice from the two-zone and CFD temperature and density plots allows a comparison to the thermocouple data of the flat flame burner. Figure 29 shows this comparison. Constraining the cold region in the two-zone model to agree with one of the

66

lines of sight that did not pass through the flame resulted in a better temperature and density determination in the hot region. Both the CFD and the two-zone model, however, give very good agreement on mole fraction in the flame. The fit compensated for the high temperature determination of the CFD model in the center by lowering the density. Once more transitions are added to the automated integration routine, the Boltzmann plots should become more accurate. This should result in better temperature agreement with both the two-zone model and the thermocouple measurements. Also, because the mole fraction in the hot region agrees with the mole fraction from the complete combustion model used in the thermocouple experiment, calculated densities should show agreement as well.
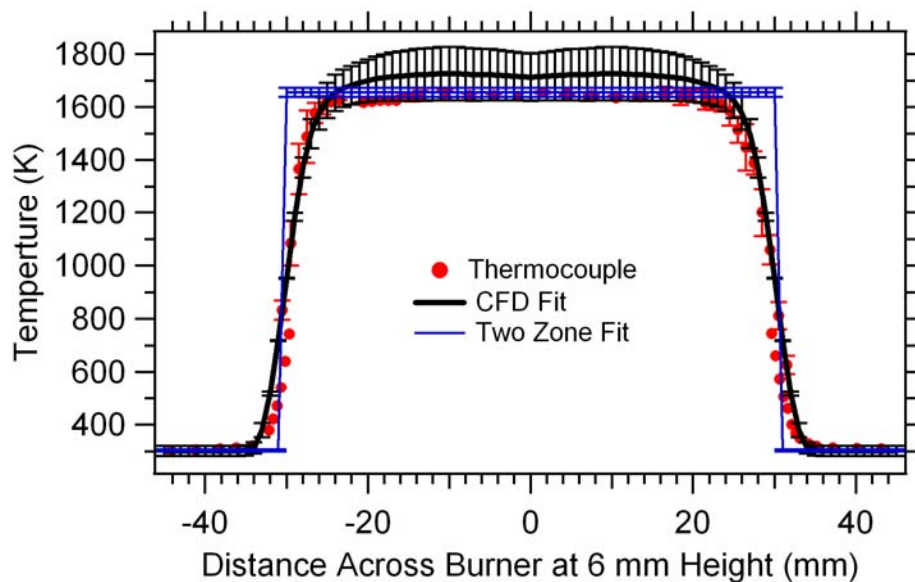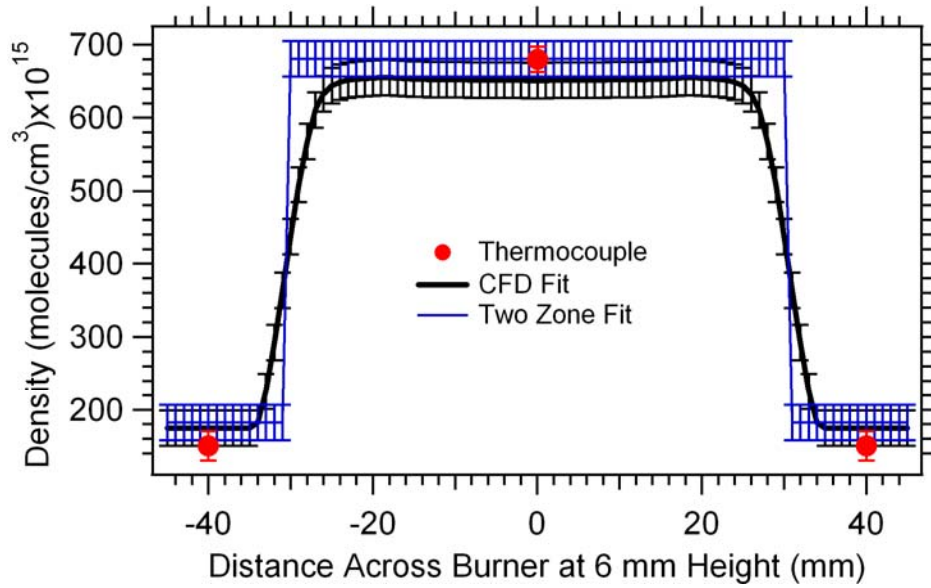
Region	PCA	Two-Zone	TC/Hum. Meter
Hot (40mm avg)	T = 1712 $\pm$ 89 K, M.F. = 0.15 $\pm$ .02	T = 1655 $\pm$ 17 K, M.F. = 0.155 $\pm$ .009	T = 1638 $\pm$ 10 K M.F. = 0.1547
Cold	T = 302 $\pm$ 19 K, M.F. = 0.0073 $\pm$ 4e-4	T = 302 $\pm$ 4 K, M.F. = 0.0076 $\pm$ 4e-4	T =300 K (Thermocouple) M.F. = 0.0061 $\pm$ 4e-4 (probe @ 293.5 $\pm$ .2 K)

Figure 29. Comparison of CFD results to two-zone results and thermocouple measurements

The strategy developed in this chapter was able to obtain accurate temperature and density measurements for the flat flame burner. The next step is to see how valuable the strategy is when applied to a more complicated flow. In Chapter VI, the same strategy and experimental setup used for the flat flame burner is employed to investigate the flow provided by the supersonic wind tunnel in Research Cell 18.

V Isolator Experiment

Introduction

This chapter serves as an introduction to the isolator experiment performed in Research Cell 18. The motivation for the flat flame burner experiment was to provide confidence in the ability of TDLAS based tomography. Its performance lends credibility to the strategy developed and its implementation in more complicated flows like that of the isolator. Paralleling the flat flame burner experiment, *a priori* information was provided by CFD calculations to reduce the number of beam paths necessary to perform tomography. However, the CFD calculations did not agree with the TDLAS data on the location of the first reflection in the shock train.   This inconsistency made it impossible to perform tomography without first adjusting the CFD calculations.   Thus, an optimization, like that of the flat flame burner diameter and center location, was performed on the isolator CFD calculations to provide a better match to the TDLAS data.

With 16 lines of sight, TDLAS was able to obtain important information about in-flow static pressure, temperature, and density before any tomography was performed. Vector quantization allowed similar conditions to be averaged to provide insight into the shock structure. This information enabled comparison with the CFD and a similar parameterization and optimization of the CFD basis images paralleling the two-zone techniques used to find diameter and center position of the flat flame burner.[16]

Isolator Experimental Setup

An identical data collection and laser control system to the system shown in Figure 11 was used to make measurements in Research Cell 18.   However, the

collimators and detectors for the laser beams were configured in metal boxes purged with nitrogen. This eliminated the water in the path up to the isolator window and allowed measurements to be made only in the region of interest. The isolator provided optical access to the vitiated, supersonic flow through small, approximately 1.5 by 3.5 inch, windows on each side. Methane was used to vitiate the flow, providing a controlled amount of water to observe using TDLAS. The backpressure of the flow was controlled by a valve downstream of the isolator. Adjusting the backpressure varied the position of the shock in the isolator which was then observed by the laser array. A diagram of the wind tunnel is shown in Figure 30. Note that the combustor in this image was replaced with a ball valve to provide the backpressure resulting in a controlled shock train.
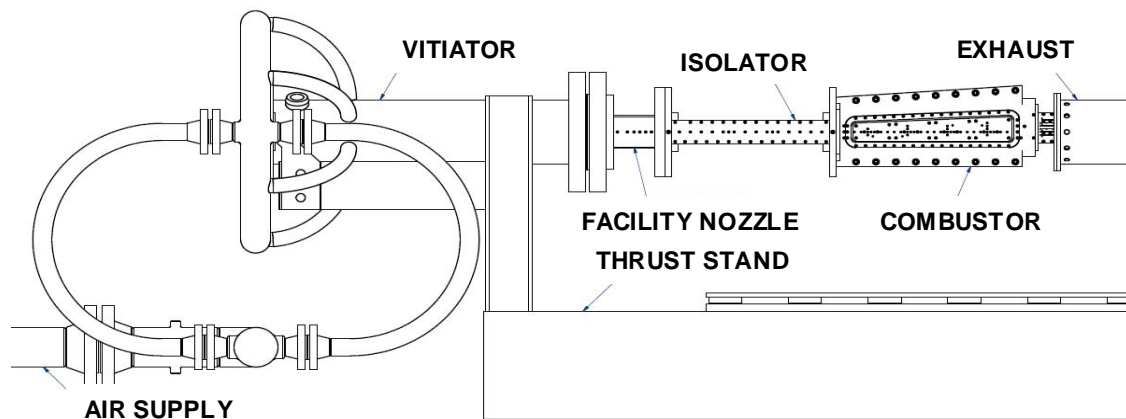
Figure 30. Schematic of the wind tunnel in RC 18 at Wright Patterson Air Force Base, adapted from reference[23]

Closing the valve increases the backpressure which pushes the shock train into and through the isolator where the laser array was able to make absorption measurements. The following plots show the CFD model of the entire isolator as the backpressure is increased.

70
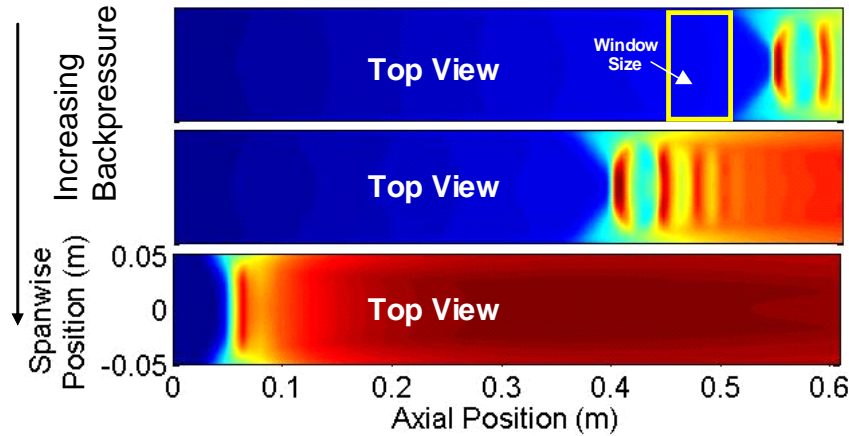
Figure 31. CFD model of shock in the isolator as backpressure is increased[3]

The image in Figure 32 shows the setup of the diode laser array. Note that this is a very similar setup to that used in the flat flame burner experiment, except the burner experiment used only one laser array and one photo-diode detector array. For the isolator experiment, eight beams were used on each side giving a total of 16 lines of sight. Two of the beams were aimed diagonally across the flow to give Doppler information and, like the angled beams in the flat flame experiment, to give tomographic information in the direction perpendicular to the flow.

71
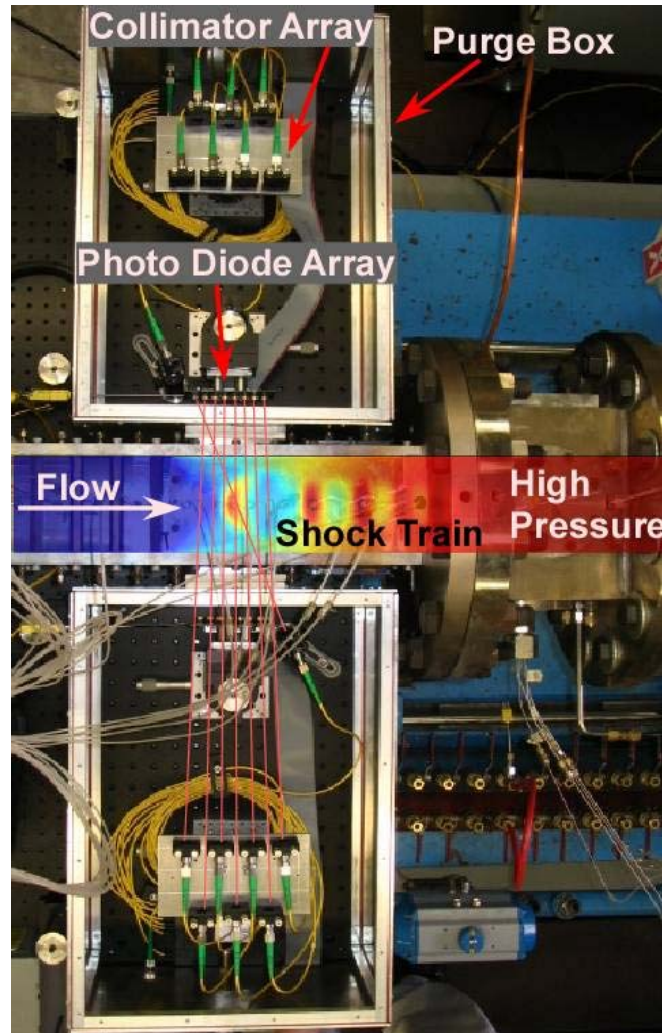
Figure 32. Image of experimental setup of laser diode and photo diode detector arrays for the isolator experiment[16]

Comparison to CFD

By integrating every spectrum at the data collection rate of 1000 Hz, instead of averaging over the entire collection like in the flat flame burner experiment, oscillations in the shock were observed. The left side of Figure 33 shows a waterfall plot of the absorption for the 14 straight lines of sight as time progressed at a constant backpressure provided by the ball valve. The vector quantization algorithm, originally intended to aid in training set dimensionality reduction, was used here to find similarly shaped plots of

the absorption across the window. By taking the average of these similar plots, the shock front and first reflection, which are the first and second pressure peaks in the shock train, were resolved as shown in the two plots on the right of Figure 33.[16]
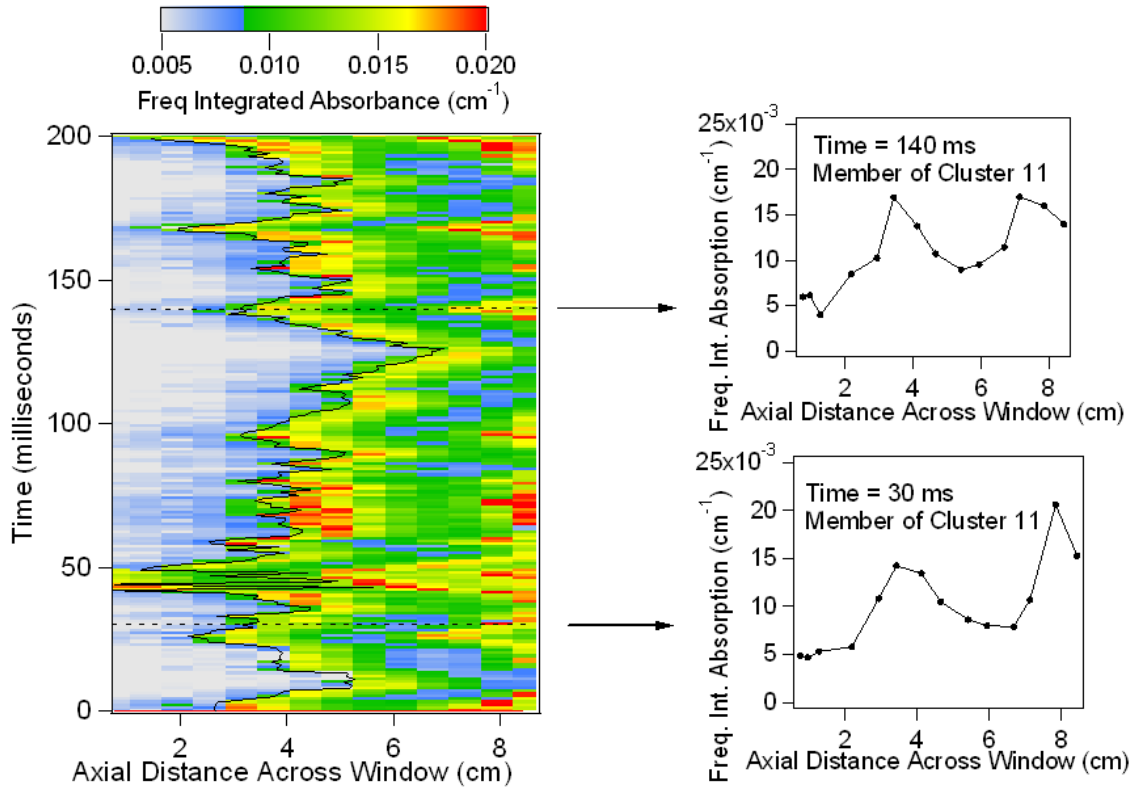
Figure 33. Waterfall plot and vector quantized averages showing shock structure in the isolator

Converting the plots in Figure 33 to pressure and temperature allows a comparison with the CFD model. The plots in Figure 34 show that the CFD is missing the first reflection in the shock train. Using the data from only 14 lines of sight perpendicular to the flow, this discrepancy in the CFD is readily apparent. Even without tomography, enough contour information is available from the TDLAS to make a comparison with the CFD calculations.

Performing tomography with a limited number of beam paths relies on contour information obtained from the CFD calculations. The discrepancy between the CFD and

73

line of sight temperatures and pressures shown in Figure 34 shows that the current CFD calculations will not provide an adequate basis function to fit the data. Tomography was, therefore, not possible using the given CFD.
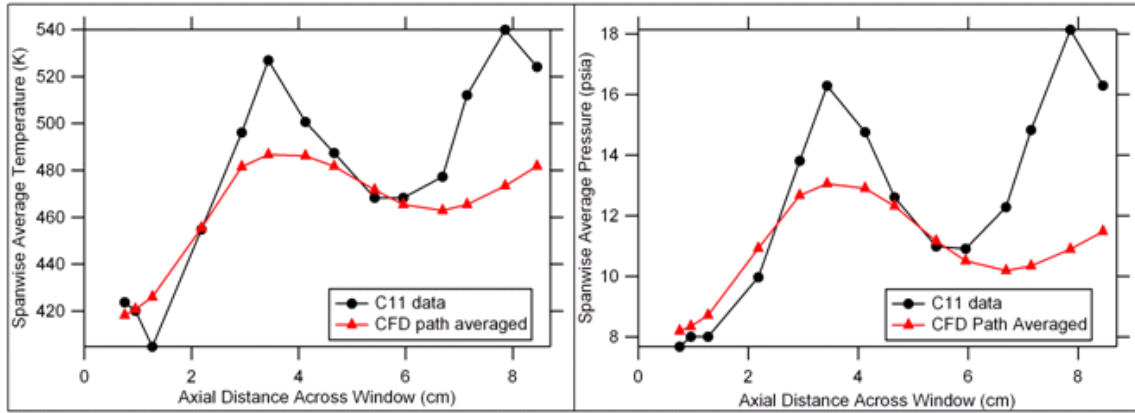
Figure 34. Averaged absorption plots converted to temperature and pressure

Optimization of CFD

By parameterizing the flow in terms of wall thickness and shock location, an optimization of the CFD was performed to correct for the missing first reflection. Similar to the scaling of the diameter of the CFD for the flat flame burner, the position of the first reflection was scaled in the isolator CFD to provide a better fit to the data as shown in Figure 35.[16]
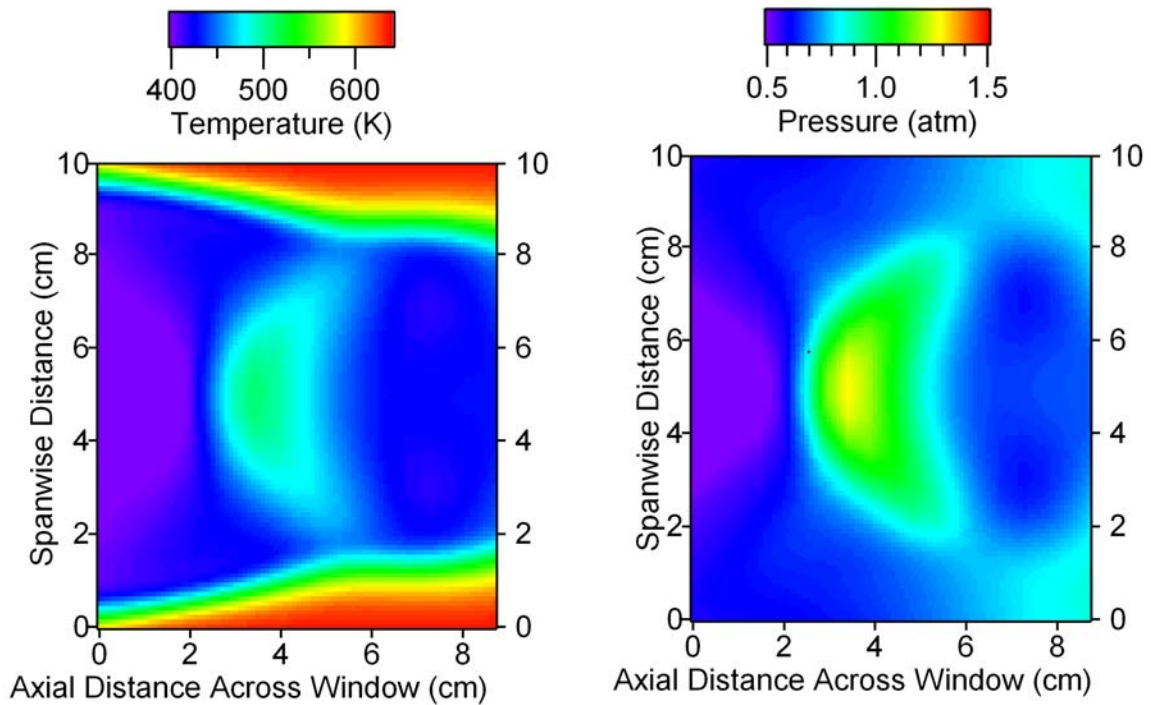
Original CFD
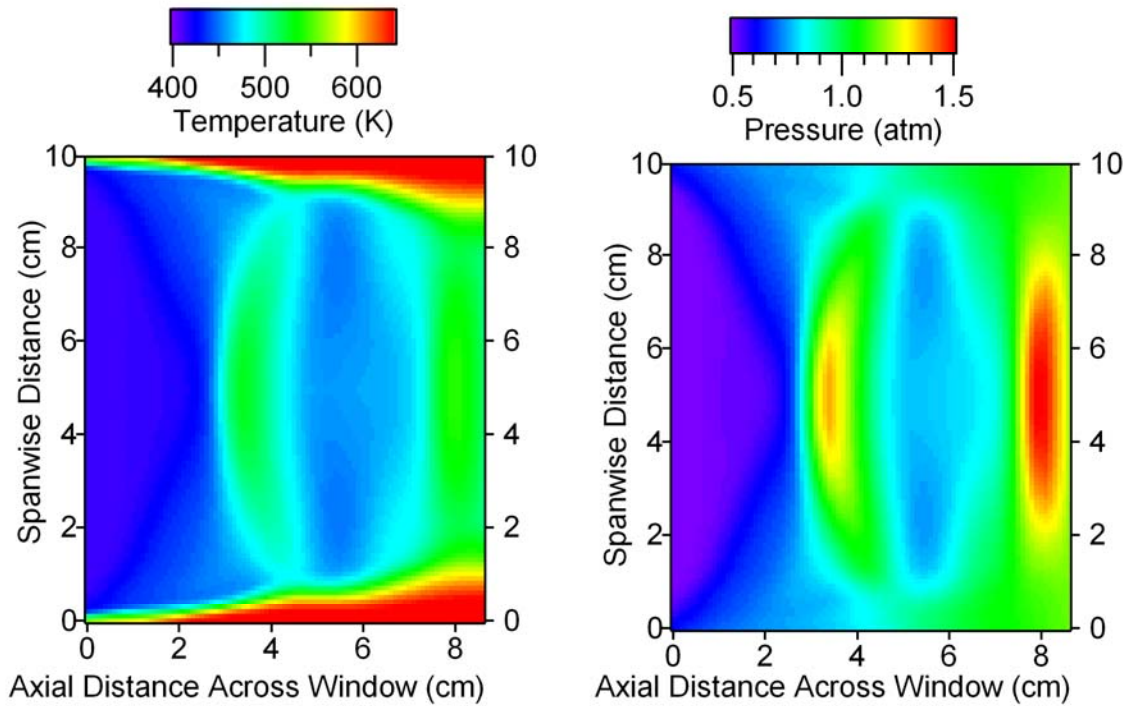
Reconstructed Images

Figure 35. Results of parameterization and optimization of CFD images to TDLAS data

The top two images show the top down view of the original CFD temperature and pressure maps for the isolator. These are the two-dimensional representations of the plots in Figure 34. Again, the first reflection is missing in both the temperature and pressure maps. After the optimization, the lowest residual was achieved by reducing thickness of the shock and moving the position of the first reflection up into the window. Enough information was available from the 16 lines of sight to enable a modification of the CFD to better fit the data. Before this experiment, CFD calculations of this sort did not have any in-flow data with which to compare. With feedback from both sides, new CFD calculations can be made, enabling better tomography which can again refine the CFD. Further implementation of the strategy presented in this thesis will put the characterization of complicated flows with limited optical access in reach.

VI Conclusions and Recommendations

The primary objective of this thesis was to provide validation of the developed strategy to perform tomography using a limited number of TDLAS beam paths. By thoroughly characterizing the flat flame burner through the traditional methods of thermocouples, pressure probes, and humidity probes, a good point of comparison was obtained. Using fairly basic geometry, the two-zone analytic method for determining temperature of the hot and cool region showed very good agreement with the thermocouple data. Applying this same model to perform tomography with varying numbers of beam paths demonstrated not only good agreement with both the two-zone analytic method and thermocouple method, but that good agreements can be achieved with very limited optical access. Finally, performing tomography with the CFD model allowed excellent determination of the contour of the burner profile as well as the mole fraction of water in the flame. By stepping through each level of tomography, this thesis shows that tomography of a flow with limited optical access is possible using TDLAS. It provides a proof of concept for the more geometrically challenging isolator experiment.

The utility of both the VQ and PCA algorithms was tested for tomography. VQ proved to be helpful in the near real-time application of tomography in the isolator. It worked very well as a method to optimize parameters in both the two-zone model and the CFD model. It was also useful in selecting similarly shaped shock structures in the time resolved shock oscillations of the isolator flow. PCA was able to reduce the CFD training sets used for the flat flame burner from 175 to just 3 images, which drastically reduced the number of beam paths necessary to perform tomography.

This thesis also demonstrated the technology necessary to perform the TDLAS measurements. Using a relatively inexpensive system, up to 16 beam paths were sampled over three spectral regions at sweep rates greater than 1 kHz resulting in 48 spectra per sweep. This high data rate allowed near real-time reconstruction of the flow in both the flat flame burner as well as the isolator.

The flat flame burner results lay the groundwork for understanding the effects of temperature changes on TDLAS based tomography. The method developed for obtaining tomographic maps of temperature and density has been carried over to the isolator experiment, where the effects of shock train structure on TDLAS based mass-flux sensors were studied. The results of the isolator experiment, introduced in Chapter 5, show that this approach can be carried over to other parts of the supersonic combustion flow path that involve complex flow distributions, such as the exhaust plane of supersonic combustors.[16]

Recommendations for future work are manifold. In the short term, a more rigorous method of automating the integration of absorption spectra is necessary. Providing more points for the Boltzmann plots should increase the accuracy of the temperature determination because now, only three points are used to perform the linear fit. Error in just one point can cause a significant difference in the temperature determination. With more points, the error will be reduced. Also, the current method for determining absorption coefficient maps fits each transition independently. Performing the fit with all of the transitions at once will help to constrain the fit and provide a more accurate result. A new flat flame burner with four independent quadrants is currently being set up. Performing the same analysis on this more complicated flow would help to

perfect the method and provide further proof of concept. Future work could also include helping to refine the CFD model by iterating on the testing of the CFD and repeating it to get a better fit.

Scheduled future work also includes flight testing of a TDLAS system on board a SCRAM Jet engine. This will provide a great deal of insight into how well TDLAS can perform in the harsh environments encountered by a supersonic vehicle. TDLAS has the potential to revolutionize the field of engine diagnostics, particularly in flight vehicles where weight and size are of critical importance.

Appendix A. Beer's Law to Frequency Integrated Absorption Coefficient

Adapted from Bernath pp 272-274.[8]

Beer's Law:

$$I = I_0 e^{-\sigma(N_0 - \frac{g_0}{g_1}N_1)l} = I_0 e^{-\sigma N_0(1 - \frac{g_0}{g_1}\frac{N_1}{N_0})l}$$

Assuming thermodynamic equilibrium, substitute in the following equations:

$$\frac{N_1}{N_0} = \frac{g_1}{g_0} e^{-h\nu_{10}/kT}$$

$$N_0 = \frac{g_0 N_T e^{-E_0/kT}}{q}$$

Then,

$$I = I_0 e^{-\sigma \frac{g_0 N_T e^{-E_0/kT}}{q}(1 - \frac{g_0}{g_1}\frac{g_1}{g_0}e^{-h\nu_{10}/kT})l} = I_0 e^{-\sigma \frac{g_0 N_T e^{-E_0/kT}}{q}(1 - e^{-h\nu_{10}/kT})l}$$

Rearrange:

$$-\ln\left(\frac{I}{I_0}\right) = \sigma \frac{g_0 N_T e^{-E_0/kT}}{q}(1 - e^{-h\nu_{10}/kT})l$$

Substitute in for the cross section:

$$\sigma = \frac{2\pi^2 S_{10}}{3\varepsilon_0 hc}\frac{\nu_{10}}{g_0}g(\nu - \nu_{10})$$

And get:

$$-\ln\left(\frac{I}{I_0}\right) = \frac{2\pi^2 S_{10}}{3\varepsilon_0 hc}\frac{\nu_{10}}{g_0}g(\nu - \nu_{10})\frac{g_0 N_T e^{-E_0/kT}}{q}(1 - e^{-h\nu_{10}/kT})l$$

But this can be simplified using the HITRAN line intensity:

$$S' = \frac{2\pi^2 \nu_{10} S_{10}}{3\varepsilon_0 hcq}e^{-E_0/kT}(1 - e^{-h\nu_{10}/kT})$$

So,

80

$$-\ln\left(\frac{I}{I_0}\right) = S'(T) \cdot N_T \cdot l \cdot g(v - v_{10}) = A = \alpha \cdot l$$

Integrate over all frequency to eliminate the line function and get:

$$\int_{-\infty}^{\infty} A(v)dv = \int_{-\infty}^{\infty} -\ln\left(\frac{I}{I_0}\right)dv = S'N_T l = \tilde{\alpha} \cdot l$$

Where $\tilde{\alpha} \cdot l$ has units of cm^{-1} if v is in wavenumbers.

Appendix B. CFD to Frequency Integrated Absorption Coefficient Map

For the flat flame burner, the CFD calculations give temperature in K, mass fraction of H_2O, and the total density of the burning gas in kg/m^3 all as a function of radial position. First, the total gas density, D_{tot}, and the mass fraction of water, F_{H2O}, are used to calculate the density of water in the flame in molecules/cm^3, N_T:

$$N_T = F_{H2O} \cdot D_{tot} \cdot \frac{1\,\text{amu}}{1.66 \times 10^{-27}\,\text{kg}} \cdot \frac{1\,H_2O\,\text{molecule}}{18.0152\,\text{amu}} \cdot \frac{1\,\text{m}^3}{10^6\,\text{cm}^3}$$

$$= F_{H2O} \cdot D_{tot} \cdot 3.34 \times 10^{19} \text{molecules}\Big/\text{cm}^3$$

Next,

$$\tilde{\alpha} = S'(T)N_T = \frac{8\pi^3 g_0 \tilde{v}_{10}}{3hcq(T_{ref})} e^{-E_0/kT_{ref}} (1 - e^{-hc\tilde{v}_{10}/kT_{ref}}) R_{10} \times 10^{-36}$$

$$\cdot \frac{q(T_{ref})}{q(T)} \frac{e^{-E_0/kT}}{e^{-E_0/kT_{ref}}} \frac{(1 - e^{-hc\tilde{v}_{10}/kT})}{(1 - e^{-hc\tilde{v}_{10}/kT_{ref}})} \cdot N_T$$

$$= S'(T_{ref}) \cdot \frac{q(T_{ref})}{q(T)} \frac{e^{-E_0/kT}}{e^{-E_0/kT_{ref}}} \frac{(1 - e^{-hc\tilde{v}_{10}/kT})}{(1 - e^{-hc\tilde{v}_{10}/kT_{ref}})} \cdot N_T$$

where $S'(T_{ref})$ has units of cm/molecule and N_T has units of molecules/cm^3, giving $\tilde{\alpha}$ units of cm^{-2}. The partition functions, q(T$_{ref}$) and q(T) are calculated using the Matlab function called partition (found in Appendix C) written by Dr. Chad Lindstrom. The line intensity, $S'(T_{ref})$, in units of cm/molecule, the term energy, E_0, and the transition energy, v_{10}, in units of wavenumbers, are given by a HITRAN table.

The following programs were written by Dr. Chad Lindstrom and Ryan Givens to

create basis functions for the flat flame burner experiment, fit the basis functions to the

data, extract temperature and density, and analyze the results:

Burnerbasisv2:

```
function [A,B,x,y] =
burnerbasis(C_list,density,temp,rratio,params,profilex,maxT)
% [B,x,y] =
% burnerbasisv2(C_list,density,temp,rratio,params,profilex,maxT)
% function to create snapshots for a McKenna burner
%
% OUTPUT:
% B = a PxQxM tensor of the M =
% numelements(C_list)*numelements(D_list)snapshots
% x = The x coordinates of the matrix
% y = The y coordinates of the matrix
%%
% INPUT:
% C_list = A Nx2 vector (x0 y0;xf yf;dx dy) that describes the range
% that the center of the burner will be moved.  It is on a square grid
% that goes from x0 to xf and y0 to yf in increments of dx and dy
%
% density = A NxM matrix consisting of a the mass fraction and density
% of the various basis guesses in the form (MF1 D1 MF2 D2 ...)
%
% temp = A Nx(M/2) matrix of the radial temperature profiles
% rratio = A list of ratios for the max water density in the flame to
% the min water density in the flame
% params = A 7x1 vector with (Lx,Ly,dx,dy,Egnd,Sref,nu) where Lx is the
% length of the  region, Ly is the length of the region in the y-
% direction, dx is the distance between adjacent pixels, dy is the
% distance between the adjacent pixels in the y-direction, Egnd is the
% ground state energy, Sref is the line intensity at 296 K, and nu is
% the wavenumber of the transition
% maxT = A list of maximum temperatures (RT is set to 293 K = 20 deg C)
%
% Author: Chad Lindstrom


Nx = floor((C_list(2,1)-C_list(1,1))/C_list(3,1))
Ny = floor((C_list(2,2)-C_list(1,2))/C_list(3,2))
NB = size(temp,2); % number of basis functions
No = size(rratio,1);
Nt = size(maxT,1);

index2 = 1;
for i=1:NB %calculate 1D absorption profiles for all cases
    for j=1:No
        for k=1:Nt
        D = density(:,2*i-1).*density(:,2*i)*3.344e19;
        maxD = D(1);
```

```matlab
            minD = maxD/rratio(j);
            D = scaleshift(maxD,minD,D);
            T = scaleshift(maxT(k),292,temp(:,i));
            A(:,index2) = alpha(T,D,params(5),params(6),params(7));
            index2 = index2+1;
            end
    end
end
index2=index2-1;

center = ones(2,1);
center(1) = C_list(1,1);
center(2) = C_list(1,2);
[H,x,y] = burnerv2(center,A(:,1),profilex,params);
L1 = size(H,1);
L2 = size(H,2);
B = ones(L1,L2,Nx*Ny*NB*No);
index = 1;

for i = 1:Nx
    for j=1:Ny
        for k=1:index2
            center(1) = C_list(1,1)+(i-1)*C_list(3,1);
            center(2) = C_list(1,2)+(j-1)*C_list(3,2);
            [H,x,y] = burnerv2(center,A(:,k),profilex,params);
            B(:,:,index) = H;
            index = index+1;
            end
        end
    end
end
```

Alpha:

```
function A = alpha(T,N,Egnd,Sref,nu)
% function A = alpha(T,N,Egnd,Sref,nu)
% is a function that calculates the integrated absorption coefficient
% map given the temperature and density maps as well as the parameters
% for the specific spectroscopic transisition
%
% Outputs:
%
%       A = the absorption map in cm^-1
%
% Inputs:
%
%       T = The temperature in Kelvin (may be a vector or matrix)
%           the maximum temperature supported is 2990 K and the minimum
%           is 200 K
%       N = The number density of the molecules (cm^-3) must be the
%           same size as T
%       Egnd = The ground state energy in cm^-1 that is being probed
%       Sref = The line intensity from Hitran at 296 K
%       nu = wavenumber of exciting light (cm^-1)
% Author: Chad Lindstrom

Qref = partition(296,nu);
Q = partition(T,nu);
S = Sref*Qref*exp(-1.439839851*Egnd*(1./T-1/300))./Q;
A = N.*S;
```

Partition:

```matlab
function Q = Partition(T,nu)
%
% function Q = Partition(T,nu)
% is a function that calculates the partition function and accounts for
% population in the excited state based on the Hitran parameters
%
%
% Outputs:
%
%       Q = The value of the partition function at temperature T (if T
%           is a vector or matrix Q will be the same size vector or
%           matrix)
%
% Inputs:
%
%       T = The temperature in Kelvin (may be a vector or matrix)
%           the maximum temperature supported is 2990 K and the minimum
%           is 200 K
%
%       nu = wavenumber of exciting light (cm^-1)
%
% Author: Chad Lindstrom

R1 = [-1.822185*10 4.230752*10^-1 7.703331*10^-4 6.185911*10^-9];
R2 = [-6.594415*10 6.945487*10^-1 2.468324*10^-4 3.484234*10^-7];
R3 = [-6.18536*10 6.973356*10^-1 2.183351*10^-4 3.699410*10^-7];
R4 = [1.993301*10^5 -4.280657*10^2 3.073247*10^-1 -7.289637*10^-5];
R5 = [-1.311914*10^3 3.214013 -1.522213*10^-3 7.885532*10^-7];
R6 = [-4.529464*10^3 7.314166 -3.265189*10^-3 1.035648*10^-6];


rows = size(T,1);
columns = size(T,2);

for i = 1:rows
    for j = 1:columns
     if (T(i,j)<=500)
         Q(i,j) = R1(1)+R1(2)*T(i,j)+R1(3)*T(i,j)^2+R1(4)*T(i,j)^3;
     elseif (T(i,j)<1000)
        Q(i,j) = R2(1)+R2(2)*T(i,j)+R2(3)*T(i,j)^2+R2(4)*T(i,j)^3;
     elseif (T(i,j)<1350)
        Q(i,j) = R3(1)+R3(2)*T(i,j)+R3(3)*T(i,j)^2+R3(4)*T(i,j)^3;
     elseif (T(i,j)<1425)
        Q(i,j) = R4(1)+R4(2)*T(i,j)+R4(3)*T(i,j)^2+R4(4)*T(i,j)^3;
     elseif (T(i,j)<2500)
        Q(i,j) = R5(1) + R5(2)*T(i,j)+R5(3)*T(i,j)^2+R5(4)*T(i,j)^3;
     else %if (T(i,j)<2990)
        Q(i,j) = R6(1) + R6(2)*T(i,j)+R6(3)*T(i,j)^2+R6(4)*T(i,j)^3;
     end
     Q(i,j) = Q(i,j)/(1-exp(-4.1357*3*nu/(8.617*T(i,j))));
    end
end
```

Scaleshift:
```
function Pn = scaleshift(P0,Pmx,data)
% function Pn = scaleshift(P0,Pmx,data)
% is a function that will scale and shift an array for the burner
% problem so that the temperatures or concentrations match measured
% values at the center and edges of the profiles
%
% Outputs:
%
%       Pn = the new profile
%
% Inputs:
%
%       P0 = The profile value at the center of the burner
%       Pmx = The profile value at the edge of the burner region
%       data = The profile(s) (each column is taken to be a profile)
%
% Author: Chad Lindstrom

columns = size(data,2);
length = size(data,1);

for i=1:columns
    x0 = data(1,i);
    xf = data(length,i);
    m = (Pmx-P0)/(xf-x0);
    b = P0-m*x0;
    Pn = data(:,i)*m+b;
end
```

burnerv2:

```
function [burnerprofile,x,y] = f(center,profile,profilex,params)
% [burnerprofile,x,y] = f(center,profile,profilex,params) function to
% create snapshots for a McKenna burner
%
% OUTPUT:
% burnerprofile = a profile that has an inner circle with magnitude
% ratio and an outer rectangular region with a value of 1
%
% x = The x coordinates of the matrix
% y = The y coordinates of the matrix
%%
% INPUT:
% center = A 2x1 vector (x0 y0) that describes the center of the burner
% profile = The 1D radial profile for the burner (assumes last point is
% absorbence coefficient in ambient air)
% profilex = The x coordinates for the burner profile
% params = A 4x1 vector with (Lx,Ly,dx,dy) where Lx is the length of
% the region, Ly is the length of the region in the y-direction, dx is
% the distance between adjacent pixels, dy is the distance between the
% adjacent pixels in the y-direction
%
% Author: Chad Lindstrom


Nx = ceil(params(1)/params(3))+1;
Ny = ceil(params(2)/params(4))+1;
x = (0:Nx-1)*params(3);
y = (0:Ny-1)*params(4);
length = size(profile,1);

burnerprofile = ones(Nx,Ny)*profile(length);
centerpixelx = center(1)/params(3);
centerpixely = center(2)/params(4);
Rpixelx = profilex(length)/params(3);
Rpixely = profilex(length)/params(4);
minpixelx = floor(centerpixelx-Rpixelx);
maxpixelx = ceil(centerpixelx+Rpixelx);
minpixely = floor(centerpixely-Rpixely);
maxpixely = ceil(centerpixely+Rpixely);
%----------Fill the snapshot matrix--------
for i = minpixelx:maxpixelx
    for j = minpixely:maxpixely
    h = sqrt((x(i)-center(1))^2+(y(j)-center(2))^2);
    %burnerprofile(i,j) = erfc((h-D/2)*1)*(ratio-1)/2+1;
    if (h<profilex(length))
        if (h>profilex(1))
        burnerprofile(i,j) = interp1q(profilex,profile,h);
        else
        burnerprofile(i,j) = interp1q(profilex,profile,profilex(2));
        end
    end
    end
end
burnerprofile = burnerprofile';
```

Create_basisv2:

```
function [basis,eig_val] = f(snapshots,mval,N)
% [basis,eig_val] = Create_basis(snapshots,mval,N) function to create
% basis from snapshots for large data sets using SVD
%
% OUTPUT:
% basis = a PxQxM tensor of M basis functions
% eig_val = an increasing vector of the eigenvalues
%
% INPUT:
% snapshots = a PxQxM tensor of the M snapshots
% mval = the mean value used to subract from snapshots
% N = number of basis elements to retain
%
% Author: Chad Lindstrom

M = size(snapshots,3); %Determine number of snapshots
rows = size(snapshots,1);

mvalv = matrixtovector(mval);
sv = matrixtovector(snapshots);
for i = 1:M
    c(i) = mvalv\sv(:,i);
    sv(:,i) = sv(:,i)-mvalv*c(i); %subract mean
end
clear mvalv;
%-----------Compute elements of Matrix to Determine Eigenvalues--------

sv = sv/sqrt(M);
[U,S,V] = svd(sv,0);
clear sv;
eig_val = diag(S.^2);
eig_val = flipud(eig_val);
for i = 1:N
    basis(:,:,i) = snapshots(:,:,1);
    basis(:,:,i) = 0;
    for j = 1:M
        basis(:,:,i) = V(j,i)*(snapshots(:,:,j)-
c(j)*mval)+basis(:,:,i);
    end
end

basis = flipdim(basis,3);
```

89

```
Matrixtovector:
function matrixtovector = f(matrix)
% matrixtovector = f(matrix) function to create vector from matrix
%
%
% OUTPUT:
% matrixtovector = either a single vector comprised of each column of
% the matrix stacked on top of each other if only one input matrix is
% given or a matrix with each column vector corresponding to each
% matrix of the 3rd rank tensor
%
% INPUT:
% matrix = either a PxQ matrix or a PxQxM tensor with M PxQ matrices
%
% Author: Chad Lindstrom


M = size(matrix,3); %Determine size of matrix
P = size(matrix,1);
Q = size(matrix,2);
matrixtovector = ones(P*Q,M);

%-----------Change matrix(es) to vector(s)--------
for i = 1:M
   for j =1:Q
       row_start = (j-1)*P+1;
       row_end = j*P;
       matrixtovector(row_start:row_end,i)=matrix(:,j,i);
   end
end
```

Datafit2:

```
Function [bestfit,resd,fiterr]=datafit(mval,basis,data,x,y,Beams,sigma)
% [bestfit,resd,fiterr] =calculatefit(mval,basis,image,x,y,Beams,sigma)
% Calculates the fit to a real data vector
%
% OUTPUT:
%
%  bestfit = the bestfit for the data
%  resd = the fit residuals
%
% Input:
%
% mval = The mean matrix
% basis = The basis used for the fit
% data = The data vector
% x = x coordinates of the image
% y = y coordinates of the image
% Beams = The beams matrix that describe the beams for inversion
% sigma = The error in the estimation of the fit integrals
%
% Author: Chad Lindstrom

[condnum,mval_proj] = Cond_Proj(Beams,mval,x,y,300);
[condnum,basis_proj] = Cond_Proj(Beams,basis,x,y,300);
%V = diag(ones(1,size(data,1))*sigma^2);
V = diag(sigma.^2);
[cm,stdcm,mse] = lscov(mval_proj,data,V);
stdcm = stdcm*sqrt(1/mse);
diff_proj = data-cm*mval_proj;
bestfit = cm*mval;
fiterr = (stdcm*mval_proj).^2;
V = diag(fiterr)+V;
[c,stdc,mse] =lscov(basis_proj,diff_proj,V);
stdc = stdc*sqrt(1/mse);
N = size(c);
bestfit = cm*mval;
fiterr = (stdcm*mval).^2;
for i=1:N
    bestfit = bestfit + c(i)*basis(:,:,i);
    fiterr = fiterr+(stdc(i)*basis(:,:,i)).^2;
end
resd = data - cm*mval_proj-basis_proj*c;
fiterr = sqrt(fiterr);

return
```

Mapthattempnew:
```
function
[tempmap,errmap,boltzmannxs,boltzmannys]=mapthattempnew(a1391_1a,a1391_
1b,a1391_2a,a1391_2b,a1391_2c,a1391_2d,a1397a,a1397b,a1397c,err1391_1a,
err1391_1b,err1391_2a,err1391_2b,err1391_2c,err1391_2d,err1397a,err1397
b,err1397c)
% mapthattempnew is a function that creates a temperature map and
% errormap using the frequency integrated absorption coefficients and
% their corresponding errors from the line of sight data using a
% Boltzmann Plot at each pixel
%
% boltzmannxs and boltzmannys are the x and y data points for the
% Boltzmann plot
%
% Author: Ryan Givens


k=.6950356;
e1391_1a=1045.0579; s1391_1a=8.335E-22;
e1391_1b=1474.9808; s1391_1b=1.131E-23;
e1391_2a=136.7617; s1391_2a=1.488E-20;
e1391_2aa=1216.1945; s1391_2aa=7.273E-23;
e1391_2b=1216.1945; s1391_2b=2.438E-22;
e1391_2c=224.8384; s1391_2c=5.577E-22;
e1391_2d=1477.2974; s1391_2d=3.277-23;
e1397a=224.8384; s1397a=1.168e-20;
e1397b=222.0528; s1397b=4.212e-21;
e1397c=1874.973; s1397c=5.983e-24;

x_points=[e1391_1a/k, ...
    ...e1391_1b/k, ...
    ...e1391_2a/k, ...
    e1391_2b/k, ...
    ... e1391_2c/k, ...
    ...e1391_2d/k, ...
    e1397a/k, ...
    ...e1397b/k, ...
    ...e1397c/k ...
    ];

v1391_1a=7185.59731;
v1391_1b=7185.40077;
v1391_2a=7181.15578;
v1391_2aa=7181.09528;
v1391_2b=7179.75201;
v1391_2c=7180.39972;
v1391_2d=7180.61301;
v1397a=7161.4101;
v1397b=7160.23543;
v1397c=7160.8121;

a1391_2a=a1391_2a-(s1391_2aa/s1391_2b).*a1391_2b; %correct for
unresolved line

boltz_map1391_1a=log(a1391_1a/s1391_1a*exp(-e1391_1a/k/300)*(1-exp(-
v1391_1a/k/300)));
```

```matlab
boltz_map1391_1b=log(a1391_1b/s1391_1b*exp(-e1391_1b/k/300)*(1-exp(-
v1391_1b/k/300)));
boltz_map1391_2a=log(a1391_2a/s1391_2a*exp(-e1391_2a/k/300)*(1-exp(-
v1391_2a/k/300)));
boltz_map1391_2b=log(a1391_2b/s1391_2b*exp(-e1391_2b/k/300)*(1-exp(-
v1391_2b/k/300)));
boltz_map1391_2c=log(a1391_2c/s1391_2c*exp(-e1391_2c/k/300)*(1-exp(-
v1391_2c/k/300)));
boltz_map1391_2d=log(a1391_2d/s1391_2d*exp(-e1391_2d/k/300)*(1-exp(-
v1391_2d/k/300)));
boltz_map1397a=log(a1397a/s1397a*exp(-e1397a/k/300)*(1-exp(-
v1397a/k/300)));
boltz_map1397b=log(a1397b/s1397b*exp(-e1397b/k/300)*(1-exp(-
v1397b/k/300)));
boltz_map1397c=log(a1397c/s1397c*exp(-e1397c/k/300)*(1-exp(-
v1397c/k/300)));


weight_map1391_1a=a1391_1a./err1391_1a;
weight_map1391_1b=a1391_1b./err1391_1b;
weight_map1391_2a=a1391_2a./err1391_2a;
weight_map1391_2b=a1391_2b./err1391_2b;
weight_map1391_2c=a1391_2c./err1391_2c;
weight_map1391_2d=a1391_2d./err1391_2d;
weight_map1397a=a1397a./err1397a;
weight_map1397b=a1397b./err1397b;
weight_map1397c=a1397c./err1397c;


tempmap=ones(size(a1397a));
errmap=tempmap;

boltzmannxs=x_points;
boltzmannys=ones(size(a1397a,1),size(a1397a,2),length(x_points));

for i=1:size(a1397a,1)
    for j=1:size(a1397a,2)
        y_points=[boltz_map1391_1a(i,j), ...
            ...boltz_map1391_1b(i,j), ...
            ...boltz_map1391_2a(i,j), ...
            boltz_map1391_2b(i,j), ...
            ...boltz_map1391_2c(i,j), ...
            ...boltz_map1391_2d(i,j), ...
            boltz_map1397a(i,j), ...
            ...boltz_map1397b(i,j), ...
            ...boltz_map1397c(i,j) ...
            ];
        weights=[weight_map1391_1a(i,j), ...
            ...weight_map1391_1b(i,j), ...
            ...weight_map1391_2a(i,j), ...
            weight_map1391_2b(i,j), ...
            ...weight_map1391_2c(i,j), ...
            ...weight_map1391_2d(i,j), ...
            weight_map1397a(i,j), ...
            ...weight_map1397b(i,j), ...
            ...weight_map1397c(i,j), ...
            ];
        S=[ones(length(x_points),1), x_points'];
```

93

```matlab
            [p,se,sd]=lscov(S,y_points',weights');
            tempmap(i,j)=-1/(p(2));
            errmap(i,j)=1/(p(2))^2*se(2);
            boltzmannys(i,j,:)=y_points;
            %tempmap(180,100)
        end
    end
```

Reperr2:

```matlab
function [maxerr,avgerr,cmean] = reperr2(B,basis,mval,nb)
% [maxerr,avgerr,cmean] = reperr2(B,basis,mval,nb)
%
%
% OUTPUT:
% maxerr = the maximum absolute percent error observed for all elements
% of the training set
%
% avgerr = the average absolute percent error observed for all elements
% of the training set
% cmean = the mean value of the expansion coefficients
%
% INPUT:
% B = a PxQxM tensor of snapshots (training set)
% basis = a PxQxM tensor of basis elements created from B
% nb = the number of basis elements to retain (the largest
%
% Author: Chad Lindstrom

Bv = matrixtovector(B);
basisv = matrixtovector(basis);
mvalv = matrixtovector(mval);
length1 = size(basisv,2);
length2 = size(Bv,2);
cmean = ones(length1,1);
cmean = 0;
avgerr = [0 0];
maxerr = [0 0];

for i=1:length2
    cav = mvalv\Bv(:,i);
    Bv2 = Bv(:,i) - cav*mvalv;
    c = basisv(:,length1-nb+1:length1)\Bv2;
    cmean = cmean+abs(c);
    result = basisv(:,length1-nb+1:length1)*c+cav*mvalv;
    abspererror = abs(Bv(:,i)-result)*100./abs(Bv(:,i));
    mr = max(abspererror);
    if (mr>maxerr(1))
        maxerr = [mr i];
    end
    avr = mean(abspererror);
    if (avr>avgerr(1))
        avgerr = [avr i];
    end
end
cmean = cmean/length2;
```

Create_VQbasis:

```matlab
function [basis,which]=f(snapshots,initial_codebook,N,epsilon)
% [basis,which] = Create_VQbasis(snapshots,initial_codebook,N,epsilon);
% function to create basis from snapshots for large data
%
% OUTPUT:
% basis = a PxQxM tensor of M basis functions
% which = a 1XM vector indicating which codevector each training set
% image is associated with
%
% INPUT:
% snapshots = a PxQxM tensor of the M snapshots
% initial_codebook = PxQxN tensor of initial codevectors
% N = number of basis elements desired
% epsilon = distortion measure (small number by which to adjust average
% basis vectors
%
% Author: Ryan Givens



M = size(snapshots,3); %determines the number of snapshots given
T = size(initial_codebook,3); %determines the number of initial
% codevectors


c = initial_codebook;



%Begin the algorithm

    D_avg_i = 5;
    D_avg_i2 = 0;

while abs((D_avg_i-D_avg_i2)/D_avg_i) > epsilon       %Continue while
% the change in relative error is still greater than epsilon
    for m = 1:M                     %Compare each image to each codevector
% and to determine which codevector the image belongs to
        difference = zeros(size(snapshots,1),size(snapshots,2),1);
        min_dif = zeros(1,T);
        for n = 1:T
            difference(:,:,n) = abs(snapshots(:,:,m)-c(:,:,n));
            min_dif(n) = ...
dot(reshape(difference(:,:,n),[],1),reshape(difference(:,:,n),[],1));
        end
        approx(:,:,m) = c(:,:,find(min_dif==min(min_dif))); %build an
% image set with the selected codevectors approximating snapshots
        which_c(m) = find(min_dif==min(min_dif));
    end
    for n = 1:T
        c(:,:,n) = ...
sum(snapshots(:,:,find(which_c==n)),3)/size(find(which_c==n),2);
    end
    D_avg_i2 = D_avg_i;
    D_avg_i = 0;
    for p = 1:M          %Find the error associated with the
% approximated image set
```

96

```
        D_avg_i = D_avg_i+dot(reshape((snapshots(:,:,M) ...
-approx(:,:,m)),1,[]),reshape((snapshots(:,:,M)-approx(:,:,m)),1,[]));
    end

    D_avg_i = 1/M/(size(snapshots,1)*size(snapshots,2))*D_avg_i;
end

basis = c;
which = which_c;
```

Bestratio:

```matlab
function [bestratio,ratiostotry,sumresd]=bestratio(R,C_list, ...
density,T,rratio,maxT,params,data,Beams)
% function to determine the amount by which to scale the cfd radius
% It returns the ratio which had the smallest residual when fit to the
% data.
%
% Author: Ryan Givens

ratiostotry=(75:125)./100;
sumresd=ones(1,length(ratiostotry));

for i=1:length(ratiostotry)
    i
    [A,B,x,y]=burnerbasisv2(C_list,density,T,rratio,params,R* ...
ratiostotry(i),maxT);
    m=mean(B,3);
    [basis,eig]=Create_basisv2(B,m,2);
    [fit,resd,err]=datafit2(m,basis,data(:,1),x,y,Beams,data(:,2));
    sumresd(i)=sum(resd.^2);
end
figure(8009)
plot(ratiostotry,sumresd)
b=find(sumresd==min(sumresd));
bestratio=ratiostotry(b);
```

Densmap:

```matlab
function [nmap,nerrmap]=densmap(fit,fiterr,tmap,terrmap)
% function to create a density map from the temperature map.  Errors
% are propogated to the nerrmap
%
% Author: Ryan Givens

Sref=1.168e-20;
nu=7161.4101;
k=.695036;
E0=224.838;
nmap=ones(size(fit));
nerrmap=nmap;

for i=1:size(fit,1)
    for j=1:size(fit,2)
        S=Sref*partition(300,nu)/partition(tmap(i,j),nu)* ...
            exp(-E0/k/tmap(i,j))/exp(-E0/k/300)*(1-exp(- ...
            nu/k/tmap(i,j)))/(1-exp(-nu/k/300));
        nmap(i,j)=fit(i,j)/S;
        nerrmap(i,j)=abs(fiterr(i,j)/S-fit(i,j)*(Sref* ...
            partition(300,nu)/exp(-E0/k/300)/(1-exp(-nu/k/300))*...
            exp(-E0/k/tmap(i,j))/partition(tmap(i,j),nu))^-...
            2*partition(tmap(i,j),nu)*exp(-E0/k/tmap(i,j))*...
            E0/k/(tmap(i,j))^2/(partition(tmap(i,j),nu))^2*Sref*...
            partition(300,nu)/exp(-E0/k/300)/(1-exp(- ...
            nu/k/300))*terrmap(i,j));
    end
end
```

Tophatfixedcold:

```matlab
function
[basis,resdmap,x,y]=tophat(centers,diameters,params,data1397,...
     Beams,sigma)
%function to create an optimized two zone basis image with the cold
%region fit only to beam paths not passing through the flame.
%
%input:
%centers: array of center locations about 0 to try
%diameters: array of diameters to try
%params: [Lx,Ly,dx,dy]
%a1397: 1397 integrated absorptions
%Beams: Beam positions
%sigma: errors in integrated absorptions
%
%Output:
%resdmap: 2D map of sum(abs(resdiduals))
%
%Author: Ryan Givens


resdmap=ones(length(centers)-1,length(diameters));
normpathlength=sqrt((Beams(1,1,1)-Beams(1,2,1))^2 ...
        +(Beams(2,1,1)-Beams(2,2,1))^2);
for i=1:length(centers)-1
    i
    for j=1:length(diameters)
        [basisa,x,y]=burner([centers(i),centers(length(centers))],...
            diameters(j),2,params);
        [basisb,x,y]=burner([centers(i),centers(length(centers))],...
            diameters(j),1,params);
        basisc=basisa-basisb;
        basisc(:,:,2)=basisa-2*basisc(:,:,1);
        %get cold basis function

basiscold=basisc(:,:,2)*(data1397(1)+data1397(7))/2/normpathlength;
        %get projection matrix (integrated area of cold path length of
each
        %path)
        [cond,projmat]=Cond_Proj(Beams,basiscold,x,y,300);
        %subtract out cold contribution to integrated absorptions
        temp_abs=data1397-projmat;
        %get hot basis function
        basishot=basisc(:,:,1);
        %fit to hot basis function
        [bestfit,resd,fiterr] = ...
            datafit3(basishot,temp_abs,x,y,Beams,sigma);
        %bestfits_arr(:,:,i)=bestfit+basiscold;


        %
[basisa,x,y]=burner([centers(i),centers(length(centers))],diameters(j),
2,params);
        %
[basisb,x,y]=burner([centers(i),centers(length(centers))],diameters(j),
1,params);
        %  basis=basisa-basisb;    %top
        %  basis(:,:,2)=basisa-2*basis(:,:,1); %bottom
```

100

```matlab
                    %
[bestfit,resd,fiterr]=datafit3(basis,data1397,x,y,Beams,sigma);
        resdmap(i,j)=sum(sum(abs(resd)));
    end

end

x=diameters;
y=centers(1:length(centers)-1);
[centerfit,diameterfit]=find(resdmap==min(min(resdmap)));
bestcenter=[centers(centerfit),centers(length(centers))]
bestdiameter=diameters(diameterfit)
[basisa,x,y]=burner(bestcenter,bestdiameter,2,params);
[basisb,x,y]=burner(bestcenter,bestdiameter,1,params);
basis=basisa-basisb;
basis(:,:,2)=basisa-2*basis(:,:,1);
```

Bibliography

1.   Hanson, M.P.A.a.R.K., *Absorption measurements of water-vapor concentration, temperature, and line-shape parameters using a tunable InGaAsP diode laser.* Applied Optics, 1993. **32**(30): p. 6104-6116.

2.   Andreadis, D., *Scramjets integrate air and space.* Industrial Physicist, 2004. **10**(4): p. 24-27.

3.   Lindstrom, C., et al. *Diode Laser Absorption Tomography of 2D Supersonic Flow*. in *43rd AIAA/ASME/SAE/ASEE Joint Propulsion Conference & Exhibit*. 2007. Cincinnati, Ohio: AIAA.

4.   Chung, K.B.G., F.C.; Wolga, G.J., *Experimental reconstruction of the spatial density distribution of a nonreacting flow with a small number of absorption measuremetns.* Applied Optics, 1998. **34**(24): p. 5492-5500.

5.   Lay, D.C., *Linear Algebra and its Applications*. 3rd ed. 2003, Boston: Addison Wesley.

6.   *Vector Quantization.*   [cited; Available from: http://www.data-compression.com/vq.html.

7.   Wavemetrics, I. *Igor Pro 6.0.*   2007   [cited; Available from: http://www.wavemetrics.com/.

8.   Bernath, P.F., *Spectra of Atoms and Molecules*. Second ed. 2005, New York, NY: Oxford University Press.

9.   Rothman, L.S., et al., *The HITRAN 2004 molecular spectroscopic database.* Journal of Quantitative Spectroscopy & Radiative Transfer, 2005. **96**: p. 139-204.

10.   Hilborn, R.C., *Einstein coefficients, cross sections, f values, dipole moments, and all that.* American Journal of Physics, 1981. **50**(11): p. 982-986.

11.   Rothman, L.S., et al., *The HITRAN molecular spectroscopic database and HAWKS (HITRAN atmospheric workstation): 1996 edition.* J. Quant. Spectrosc. Radiat. Transf., 1998. **60**: p. 665-710.

12.   Sanders, S.T., et al., *Diode-laser absorption sensor for line-of-sight gas temperature distributions.* Applied Optics, 2001. **40**(24): p. 4404-4415.

13.   Gamache, R.R., Kennedy, S., Hawkins, R., Rothman, L.S., *Total Internal Partition Sums for Molecules in the Terrestrial Atmosphere.* Journal of Molecular Structure, 1999(517-518): p. 407-425.

14.   Torniainen, E.D., A.K. Hinz, and F.C. Gouldin, *Tomographic Analysis of Unsteady, Reacting Flows: Numerical Investigation.* AIAA Journal, 1998. **36**(7): p. 1270-1278.

15.   Metacomp. *http://www.metacomptech.com/index.html*. 2006 [cited; Available from: http://www.metacomptech.com/index.html.

16.   Lindstrom, C., et al., *Diode laser absorption tomography using data compression techniques*, in *SPIE Electronic Imaging Conference*. 2008.

17.   Torniainen, E.D. and F.C. Gouldin, *Tomographic Reconstruction of 2-D Absorption Coefficient Distributions from a Limited Set of Infrared Absorption Data.* Combust. Sci. and Tech., 1998. **131**: p. 85-105.

18.   Kasap, S.O., *Thermoelectric Effects in Metals: Thermocouples*. 2001.

19.   Blevins, L.G.P., William M, *Modeling of bare and aspirated thermocouples in compartment fires.* Fire Safety Journal 1999. **33**: p. 239-259.

20.   Brohez, S.D., C.; Marlair, G., *A two-thermocouples probe for radiation corrections of measured temperatures in compartment fires.* Fire Safety Journal, 2004. **39**: p. 399-411.

21.   Shaddix, C.R. *Correcting thermocouple measurements for radiation loss: A critical review*. in *33rd National Heat Transfer Conference*. 1999. Albuquerque, NM.

22.   Weigand, P., R. Luckerath, and W. Meier. *Documentation of Flat Premixed Laminar CH_4/Air Standard Flames: Temperatures and Species Concentrations*. 2006 [cited; Available from: http://www.dlr.de/vt/PortalData/29/Resources/dokumente/ch4_air_flames.pdf.

23.   Williams, S., et al., *Diode Laser Diagnostics of High Speed Flows*, in *14th AIAA/AHI International Space Planes and Hypersonic Systems and Technologies Conference*. 2006: Canberra, Australia.

24.   Humlíček, J., *Optimized Computation of the Voigt and Complex Probability Functions.* J. Quant. Spectrosc. Radiat. Transfer, 1982. **27**(4): p. 437-444.

REPORT DOCUMENTATION PAGE

Form Approved
OMB No. 0704-0188

The public reporting burden for this collection of information is estimated to average 1 hour per response, including the time for reviewing instructions, searching existing data sources, gathering and maintaining the data needed, and completing and reviewing the collection of information. Send comments regarding this burden estimate or any other aspect of this collection of information, including suggestions for reducing the burden, to the Department of Defense, Executive Services and Communications Directorate (0704-0188). Respondents should be aware that notwithstanding any other provision of law, no person shall be subject to any penalty for failing to comply with a collection of information if it does not display a currently valid OMB control number.
PLEASE DO NOT RETURN YOUR FORM TO THE ABOVE ORGANIZATION.

1. REPORT DATE *(DD-MM-YYYY)*	2. REPORT TYPE	3. DATES COVERED *(From - To)*
27-03-2008	Master's Thesis	Jun 2007 - Mar 2008

4. TITLE AND SUBTITLE

Demonstration of a Strategy to Perform Two-Dimensional Diode Laser Tomography

5a. CONTRACT NUMBER

5b. GRANT NUMBER

5c. PROGRAM ELEMENT NUMBER

6. AUTHOR(S)

Givens, Ryan N., Captain, USAF

5d. PROJECT NUMBER

5e. TASK NUMBER

5f. WORK UNIT NUMBER

7. PERFORMING ORGANIZATION NAME(S) AND ADDRESS(ES)

Air Force Institute of Technology
Graduate School of Engineering Management (AFIT/EN), 2950 Hobson Way
WPAFB, OH 45433-7765

8. PERFORMING ORGANIZATION REPORT NUMBER

AFIT/GAP/ENP/08-M04

9. SPONSORING/MONITORING AGENCY NAME(S) AND ADDRESS(ES)

Dr. Skip Williams
Air Force Research Laboratory, Propulsions Directorate
1950 Fifth Street
WPAFB, OH 45431-7251

10. SPONSOR/MONITOR'S ACRONYM(S)

AFRL/RZAS

11. SPONSOR/MONITOR'S REPORT NUMBER(S)

12. DISTRIBUTION/AVAILABILITY STATEMENT

APPROVED FOR PUBLIC RELEASE; DISTRIBUTION UNLIMITED

13. SUPPLEMENTARY NOTES

14. ABSTRACT

Demonstration of a strategy to perform two-dimensional diode laser tomography using a priori knowledge from symmetry arguments and computational fluid dynamic (CFD) calculations is presented for a flat flame burner. The strategy uses an optimization technique to determine flame diameter and location using a vector quantization approach. Next, the variance in a training set, produced from CFD calculations, is captured using principal components analysis. The information in the training set allows interpolation between beam paths resulting in temperature and density maps. Finally, the TDLAS temperature and density maps are shown to agree with traditional thermocouple measurements of the flat flame burner to within five percent. Preliminary tomography results using the same strategy are then presented for a super-sonic flow through an isolator, a length of wind tunnel necessary to keep the shock wave produced by the combustor from reaching the inlet.

15. SUBJECT TERMS

Tunable Diode Laser Absorption Spectroscopy (TDLAS), Tomography, Vector Quantization (VQ), Principal Components Analysis (PCA)

16. SECURITY CLASSIFICATION OF:			17. LIMITATION OF ABSTRACT	18. NUMBER OF PAGES	19a. NAME OF RESPONSIBLE PERSON
a. REPORT	b. ABSTRACT	c. THIS PAGE			William F. Bailey (ENP)
U	U	U	UU	119	19b. TELEPHONE NUMBER *(Include area code)* (937)255-3636 X 4501, william.bailey@afit.edu

Standard Form 298 (Rev. 8/98)
Prescribed by ANSI Std. Z39.18